Lithos 114 (2010) 293–306

Contents lists available at ScienceDirect

Lithos

journal homepage: www.elsevier.com/locate/lithos

Miocene high Sr/Y magmatism, south Tibet: Product of partial melting of subducted Indian continental crust and its tectonic implication

Wang-Chun Xu [a], Hong-Fei Zhang [a,*], Liang Guo [a], Hong-Lin Yuan [b]

[a] State Key Laboratory of Geological Process and Mineral Resources, China University of Geosciences, Wuhan 430074, PR China
[b] State Key Laboratory of Continental Dynamics, Northwest University, Xi'an, 710069, PR China

ARTICLE INFO

Article history:
Received 28 March 2009
Accepted 16 September 2009
Available online 28 September 2009

Keywords:
High Sr/Y rock
Petrogenesis
Magma source
Continental subduction
Lhasa terrane

ABSTRACT

Post-collisional (26–10 Ma) high Sr/Y and HREE-depleted intrusive rocks occur in an E–W trending belt paralleling the Yarlung–Zangbo suture in south Tibet. Their petrogenesis has been a subject of debate. Here, we present chronological, geochemical and Sr–Nd–Hf isotopic data for two newly discovered large-volume high Sr/Y granitoids (the Pagu granodiorite and the Nanmuqie granite) and three high Sr/Y porphyries intruding the granitoids in the Lhasa terrane. LA-ICP-MS zircon U–Pb dating for the Pagu granodiorite and Nanmuqie granite yielded identical magma crystallization ages of 14.0–14.4 Ma, which is indistinguishable from their associated high Sr/Y porphyries (14.2–14.6 Ma). The granitoid was intruded at middle-crust depth, whereas the porphyry was intruded at upper-crust depth, indicating that the Lhasa terrane has experienced a rapid crustal uplift during the high Sr/Y magma emplacement. Zircon Hf isotopic and whole-rock Sr–Nd isotopic compositions for these granitoids and porphyries suggest that their magmas were dominantly derived from partial melting of crustal materials. The granitoids and porphyries have $\varepsilon_{Hf}(t)$ values overlapping with the mafic granulites in the Himalayan terrane (Indian plate). Their Sr–Nd isotopic compositions show two-endmember mixing between the Himalayan mafic lower crust and the ultrapotassic lavas/the Lhasa lower crust. We suggest that the high Sr/Y magmas in the Lhasa terrane could be derived from partial melting of subducted Indian mafic lower crust with incorporation of the ultrapotassic lava and/or the Lhasa lower crust components. Our study suggests a new model for the high Sr/Y magma generation in the Lhasa terrane and provides a line of geochemical evidence that the Indian continental crust was subducted beneath the southern Lhasa terrane in the early–middle Miocene.

1. Introduction

Tibet is the largest and highest plateau on the Earth, which has a profound impact on the regional and global climate, oceanic circulation, as well as biological and ecological migration (Edmond, 1992; Prell and Kutzbach, 1992; Raymo and Ruddiman, 1992; Molnar et al., 1993; Derry and France-Lanord, 1996; Garzione et al., 2000; An et al., 2001; Dupont-Nivet et al., 2007). The Tibetan plateau resulted from Paleocene collision and continued convergence between the Indian and Eurasian plates (Beck et al., 1995; de Sigoyer et al., 2000; Leech et al., 2005; Yin, 2006). During the convergence, whether or not the Indian continental lithosphere was subducted beneath the Tibetan plateau is a matter of debate (Powell, 1986; Zhao and Morgan, 1987; England and Houseman, 1989; Molnar et al., 1993; Tapponnier et al., 2001). Geophysical data suggest that the Indian lithosphere had been underthrusted beneath the Lhasa terrane, even as far north as the Bangong–Nujiang suture (Jin et al., 1996; Owens and Zandt, 1997; Rodgers and Schwartz, 1997; Tilmann et al., 2003; Schulte-Pelkum et al., 2005). However, geochemical data are insufficient to determine if the Indian continent was subducted beneath the Lhasa terrane. Geochemical, isotopic and chronological studies of post-collisional magmatic rocks can provide important information on the magmatic source and mantle/crust interactions, which contribute to our understanding of the continental collision process.

Since Miocene high Sr/Y and HREE-depleted porphyries, termed adakitic in some publications, in the Lhasa terrane were reported (Chung et al., 2003), several different models have been proposed for the magma generation of the porphyries (Chung et al., 2003; Hou et al., 2004; Qu et al., 2004; Gao et al., 2007). Because different petrogenetic models have distinct geologic implications, additional constrains on the age, distribution and geochemistry of the Cenozoic high Sr/Y rocks in the Lhasa terrane are necessary to distinguish their sources.

This paper presents geochronology, geochemical and Sr–Nd–Hf isotopic data for two high Sr/Y granitoids (large-volume batholith) and three porphyries intruding the granitoids from the Lhasa terrane. Our data suggest that the high Sr/Y magmas are most probably derived from partial melting of subducted Indian mafic lower crust. Our study provides new constraints on the continental structure and crustal uplift in the southern Tibet.

* Corresponding author.
E-mail address: hfzhang@cug.edu.cn (H.-F. Zhang).

0024-4937/$ – see front matter © 2009 Elsevier B.V. All rights reserved.
doi:10.1016/j.lithos.2009.09.005

2. Geologic setting and samples

The Tibetan plateau from north to south comprises E–W trending Qiangtang, Lhasa and Himalaya terranes (Fig. 1). The Lhasa terrane is bounded by the Bangong–Nujiang suture to the north and the Yarlung–Zangbo suture to the south (Fig. 1a). While its northern part remains debated (Ding et al., 2003; Kapp et al., 2003; Kapp et al., 2005; Pan et al., 2006; Zhu et al., 2006), the southern part (also called Gangdese belt) of the Lhasa terrane is considered as an Andean-type active continental margin prior to the India–Eurasian collision in early Cenozoic (Yin and Harrison, 2000; Mo et al., 2007; Wen et al., 2008). Recent studies suggested that the Neotethyan oceanic slab subduction underneath the southern margin of the Eurasian plate had started since at least Early Jurassic (Chu et al., 2006; Zhang et al., 2007a; Zhu et al., 2008). Due to the Neotethyan oceanic slab subduction and subsequent continental collision between the Indian and Eurasian plates, the voluminous Gangdese batholith and the widespread Linzizong volcanic succession formed in the southern Lhasa terrane in the Cretaceous–Early Tertiary (Yin and Harrison, 2000; Mo et al., 2003; Mo et al., 2007; Mo et al., 2008; Wen et al., 2008). After a magmatism quiescent period of ~15 Ma (40 to 25 Ma) in the southern Lhasa terrane, three types of post-collisional magmatism, including high Sr/Y intrusive rocks, potassic–ultrapotassic volcanic rocks and peraluminous granites, took place in the period from ~25 Ma to ~10 Ma (Chung et al., 2005; Liao et al., 2007; Mo et al., 2007). Among them, the ultrapotassic volcanic rocks have attracted great attention. Previous studies indicate that these ultrapotassic rocks exhibit negative Nb, Ta and Ti anomalies, strong enrichment in incompatible elements, and relatively radiogenic Sr and unradiogenic Nd isotopic compositions (Turner et al., 1996; Miller et al., 1999; Williams et al., 2001, 2004; Ding et al., 2003). Although a number of mechanisms have been proposed to explain the genesis of the ultrapotassic rocks, all of them invoke low degree of partial melting of a metasomatized lithospheric mantle (phlogopite-bearing peridotite) (Turner et al.,

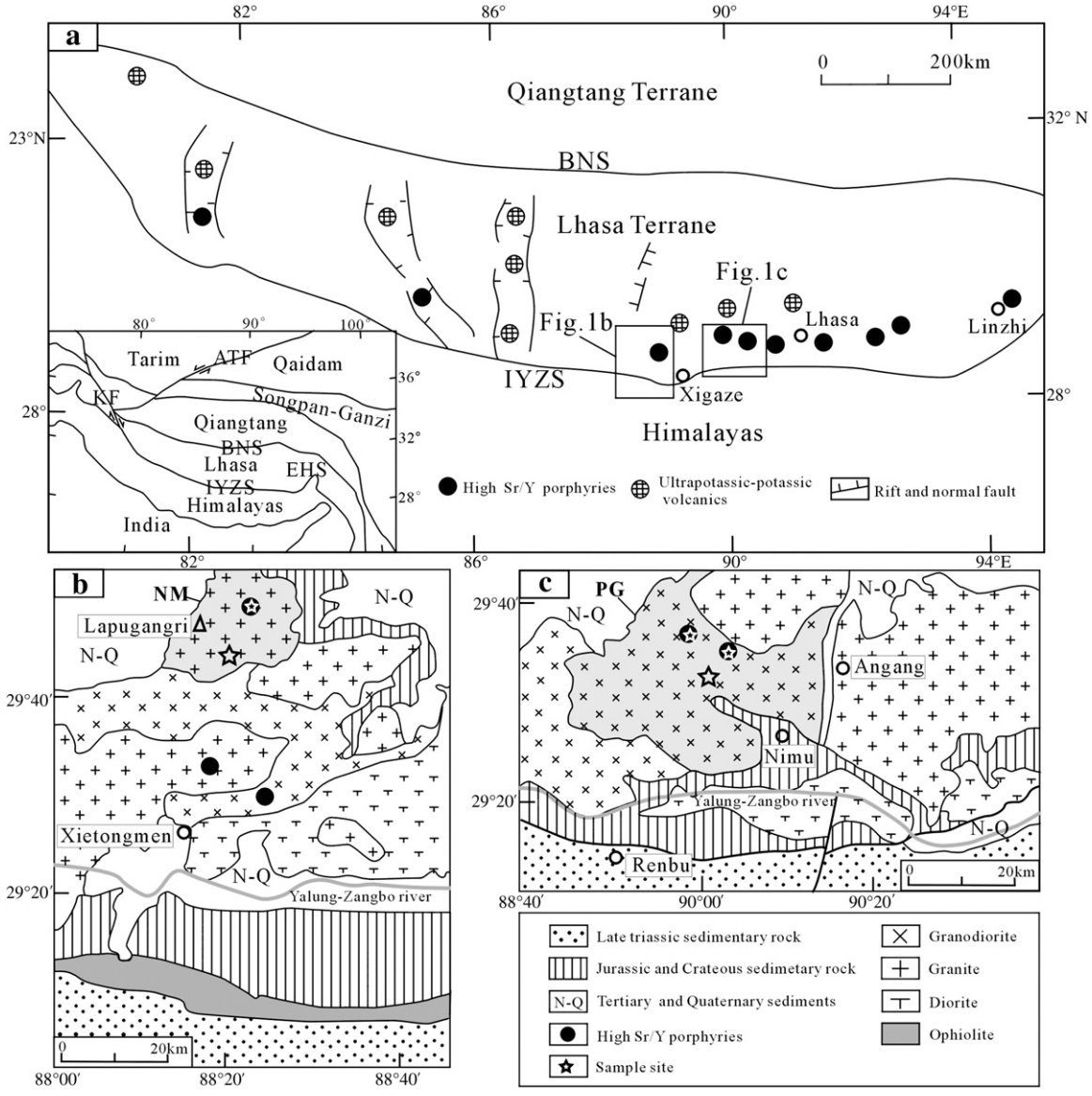

Fig. 1. (a) Distribution map of post-collisional high Sr/Y porphyries and ultrapotassic–potassic volcanic rocks in the Lhasa terrane (modified after Turner et al., 1996; Miller et al., 1999; Williams et al., 2001; Chung et al., 2003; Hou et al., 2004; Gao et al., 2007; Guo et al., 2007); inset shows the different terranes and main structures in Tibet plateau and its adjacent areas. (b) and (c) Simplified geological maps of Xietongmen area and Nimu area, respectively (modified after 1:1,500,000 geological map of Qinghai–Tibet Plateau and its adjacent areas by the Geological Survey of China). NM = the Nanmuqie granite, PG = the Pagu granodiorite. BNS = Bangong–Nujiang suture; IYZS = Indus–Yarlung–Zangbo suture; KF = Karakorum Fault; ATF = Altyn Tagh Fault; EHS = Eastern Himalayan syntaxis.

1996; Miller et al., 1999; Ding et al., 2003; Williams et al., 2001, 2004). These post-collisional magmatic rocks are locally controlled by NS-striking normal faulting systems that resulted from the east–west extension in the southern Tibet. Available age data show that the normal faulting occurred between ~18 and ~13 Ma (Coleman and Hodges, 1995; Blisniuk et al., 2001; Williams et al., 2001).

This study focuses on the petrogenesis of Cenozoic high Sr/Y intrusive rocks, involving the large-volume granitoids and the small-volume porphyries intruding the granitoids in the southern Lhasa terrane. While previous work was concerned with the high Sr/Y porphyries (Chung et al., 2003; Hou et al., 2004; Qu et al., 2004; Gao et al., 2007; Guo et al., 2007), the large-volume high Sr/Y granitoids have been unknown in the Lhasa terrane until this study. We investigate the Pagu (PG) granodiorite and Nanmuqie (NM) granite and identify them to be high Sr/Y intrusive rocks. The PG granodiorite crops out over an area of ~900 km^2. It intrudes into Upper Jurassic and Lower Cretaceous strata, and is intruded by the Chongjiang and Tinggong porphyries (Fig. 1c). The coarse-grained PG granodiorite is composed of quartz (15–22%), plagioclase (45–50%), K-feldspar (15–20%), amphibole (6–10%), biotite (3–5%) and accessory minerals (<1%) including zircon and Fe–Ti oxides. The NM granite crops out over an area of ~400 km^2. It also intrudes into Upper Jurassic and Lower Cretaceous strata, and is intruded by a small-volume porphyry (hereafter called as the NM porphyry) (Fig. 1b). The NM granite is porphyritic and contains K-feldspar phenocrysts (8–12%). Among these phenocrysts, some occur as megacrysts (>1 cm). The NM granite consists of quartz (25–30%), plagioclase (25–32%), K-feldspar (35–40%), biotite (3–5%), and accessory minerals including zircon and Fe–Ti oxides. The high Sr/Y porphyries that intrude into the PG and NM granitoids occur as stocks of <0.5 km^2. In rock type, the porphyries are granodioritic and granitic. The porphyries have porphyritic textures with 10–40% phenocrysts of plagioclase, K-feldspar, quartz and biotite.

3. Analytical methods

Major elements were measured by XRF at the State Key Laboratory of Continental Dynamics (SKLCD), Northwest University, Xi'an, China. The analytical uncertainty is usually <5%. Trace elements and rare earth elements (REE) were measured using ICP-MS at the State Key Laboratory of Geological Processes and Mineral Resources (GPMR), China University of Geosciences, Wuhan, China. The analytical precision is better than 5–10%. For the detailed analytical methods see Zhang et al. (2002).

Whole-rock Sr and Nd isotopic ratios were measured by a Triton thermal ionization mass spectrometer at GPMR. $^{87}Rb/^{86}Sr$ and $^{147}Sm/^{144}Nd$ ratios were calculated from measured Rb, Sr, Sm and Nd contents by ICP-MS. The measured Sr and Nd isotopic ratios were normalized to $^{86}Sr/^{88}Sr = 0.1194$ and $^{146}Nd/^{144}Nd = 0.7219$, respectively. During the period of analysis, NBS987 standard yielded an average $^{87}Sr/^{86}Sr$ value of 0.710239 ± 10 (2σ) and BCR-2 standard gave an average $^{143}Nd/^{144}Nd$ value of 0.512620 ± 2 (2σ). For details of the Sr and Nd isotopic analytical procedures see Gao et al. (2004).

Zircons from whole-rock samples were separated by heavy-liquid and magnetic methods and then purified by hand picking under a binocular microscope. The zircon crystals were mounted in an epoxy disc and then were polished to expose their centres. Cathodoluminescence (CL) imaging for the zircons was carried out at SKLCD. Under guidance of CL images, the zircons were analyzed for U–Th–Pb contents and isotopic compositions using LA-ICP-MS at GPMS. The laser spot is 32 μm in diameter. Helium was loaded for laser ablation. Measurements were corrected using reference zircon standard 91500 and NIST SRM610 glass. The detailed analytical procedures are given in Yuan et al. (2004). Since high purity argon and helium (>99.999%) were used, background intensities of ^{206}Pb and ^{238}U were lower than 20 counts per second (cps). During the period of analysis, all samples gave a ^{206}Pb signal of 0.6×10^4 to 4.0×10^4 cps and a ^{238}U signal of 1.0×10^6 to 4.0×10^6 cps, depending on their respective contents. The common Pb correction followed ComPbCorr#3-151 procedure (Andersen, 2002). Data processing is carried out using Isoplot (Ludwig, 2003). Because our samples are young (Cenozoic), Tera-Wasserburg Concordia plots are chosen to display the analytical data.

In-situ zircon Hf isotope analysis was subsequently performed on the dated zircon domains using LA-MC-ICP-MS at SKLCD. The laser spot is 44 μm in diameter. Helium was used as carrier gas transporting the ablated sample from the ablation cell to the ICP-MS torch. Zircon 91500, GJ-1 and Monastery were used as reference standards. The analytical procedures were reported in Yuan et al. (2008). A decay constant was adopted for ^{176}Lu of 1.865×10^{-11} $year^{-1}$ (Scherer et al., 2001). Initial $^{176}Hf/^{177}Hf$ was calculated according to the $^{206}Pb/^{238}U$ age, and the value of $\varepsilon_{Hf}(t)$, is calculated relative to the chondritic reservoir with a $^{176}Hf/^{177}Hf$ ratio of 0.282772 and $^{176}Lu/^{177}Hf$ of 0.0332 (Blichert-Toft and Albarede, 1997). Single-stage Hf model ages (T_{DM1}) are calculated relative to the depleted mantle which is assumed to have a linear isotopic growth from $^{176}Hf/^{177}Hf = 0.279718$ at 4.55 Ga to 0.283250 at present, with $^{176}Lu/^{177}Hf$ ratio of 0.0384 (Vervoort and Blichert-Toft, 1999; Griffin et al., 2000), and two-stage Hf model ages (T_{DM2}) are calculated by assuming a mean $^{176}Lu/^{177}Hf$ value of 0.015 for the average continental crust (Griffin et al., 2002).

4. Results

4.1. Zircon U–Pb geochronology

LA-ICP-MS zircon U–Pb data are listed in the supplemental electronic data table (Table A), and representative zircon CL images and their U–Pb concordia plots are shown in Figs. 2 and 3, respectively.

Two samples (T380 and T381) from the PG granodiorite were chosen for zircon U–Pb dating. Zircons from both samples are euhedral and long to short prismatic, with average crystal length being ~200 μm and length-to-width ratio of 2:1. Most zircons are transparent, colourless and show clear oscillatory zoning, indicating a magmatic origin (Fig. 2c and d) (Corfu et al., 2003). Fifteen analyses on zircon crystals from T380 yield $^{206}Pb/^{238}U$ ages between 13.5 ± 0.4 and 15.3 ± 0.6 Ma, with a weighted mean of 14.3 ± 0.3 Ma (2σ; MSWD = 1.3) (Fig. 3c). These zircons have U of 336–1001 ppm, Th of 287–1049 ppm and Th/U ratios of 0.66–1.22 (Table A). One additional analysis gives a $^{206}Pb/^{238}U$ age of 51 ± 2 Ma with low U (276 ppm) and Th (141 ppm), which could be a captured zircon. Fifteen analyses on zircon crystals from T381 yield $^{206}Pb/^{238}U$ ages between 13.2 ± 0.5 and 14.7 ± 0.6 Ma, with a weighted mean of 14.0 ± 0.3 Ma (2σ; MSWD = 0.67) (Fig. 3d). These zircons have U of 427–682 ppm, Th of 303–1129 ppm and Th/U ratios of 0.62–1.65 (Table A). No inherited or captured zircons are found in this sample. Together, the two dated samples show the same weighted mean $^{206}Pb/^{238}U$ ages of ~14 Ma, which is interpreted as the magma crystallization age of the PG granodiorite.

The Chongjiang and Tinggong porphyries intrude the PG granodiorite (Fig. 1c). Samples T339 and T358 were collected from the Chongjiang and Tinggong porphyry copper deposits, respectively. Zircons from T339 and T358 are mostly transparent, colourless and short prismatic, with average crystal length being ~150 μm and length/width ratio of 2:1. CL images display clear magmatic oscillatory zoning (Fig. 2a and b). Fourteen analyses on zircon crystals from T339 yield $^{206}Pb/^{238}U$ ages between 14.1 ± 0.4 and 15.6 ± 0.4 Ma, with a weighted mean of 14.6 ± 0.3 Ma (2σ; MSWD = 1.3) (Fig. 3a), which is close to the SHRIMP zircon U–Pb age of 15.6 ± 0.5 Ma obtained by Hou et al. (2004). One analysis produces an older $^{206}Pb/^{238}U$ age of 24.1 ± 0.6 Ma. Apart from one with abnormally high U and Th contents (U = 1444 ppm and Th = 6326 ppm), fourteen analyses have U of 374–967 ppm, Th of 287–1017 ppm and Th/U ratios of 0.77–4.38 (Table A). For sample T358, sixteen analyses on zircon crystals

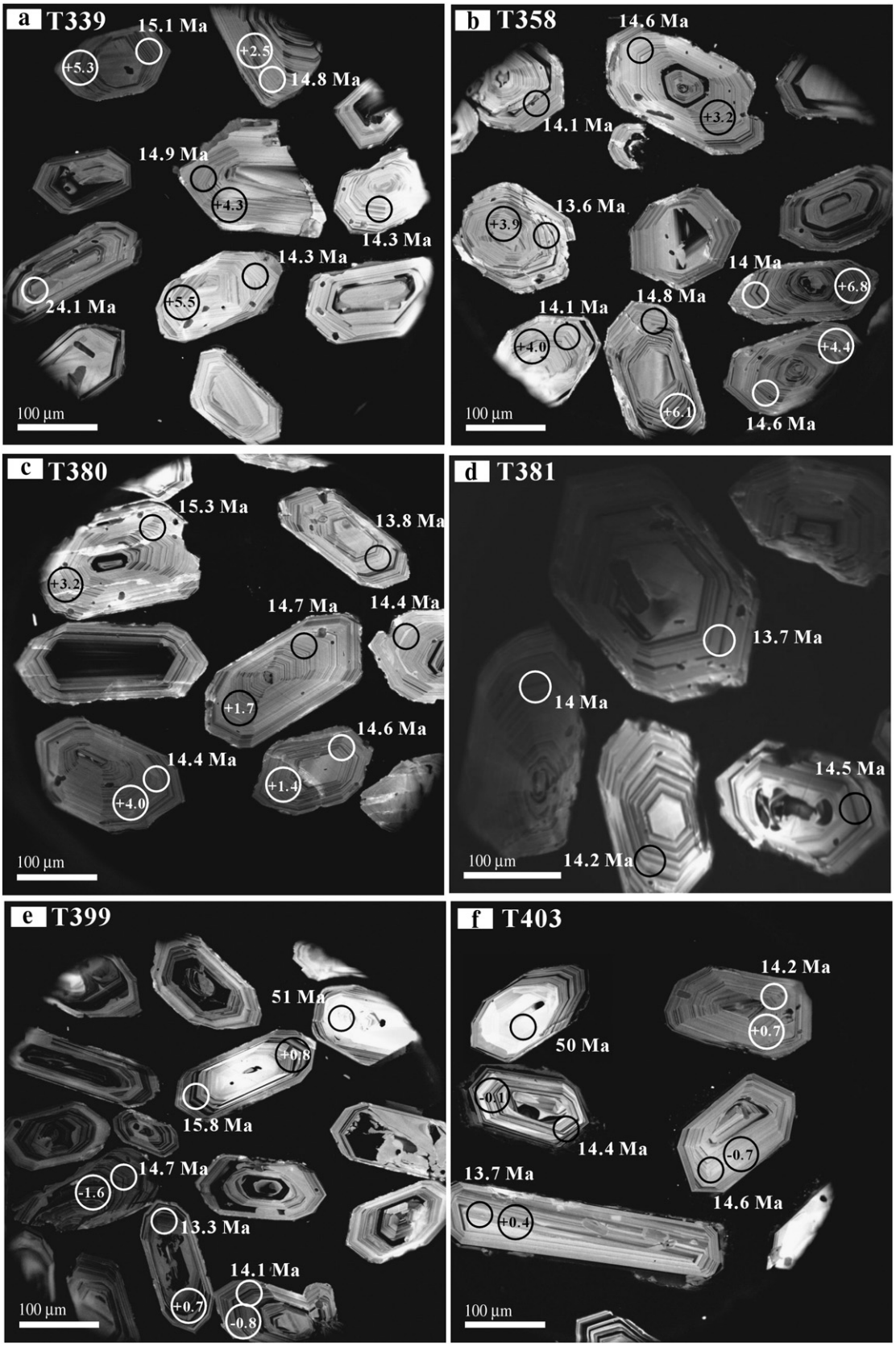

Fig. 2. Representative CL images. The smaller circles show LA-ICP-MS dating spots and corresponding $^{206}Pb/^{238}U$ apparent ages, and the bigger circles show locations of Lu–Hf isotope analysis and corresponding $\varepsilon_{Hf}(t)$ values. (a) Chongjiang porphyry (sample T339); (b) Tinggong porphyry (sample T358); (c) and (d) Pagu granodiorite (sample T380 and T381); (e) Nanmuqie porphyry (sample 399); (f) Nanmuqie granite (sample T403).

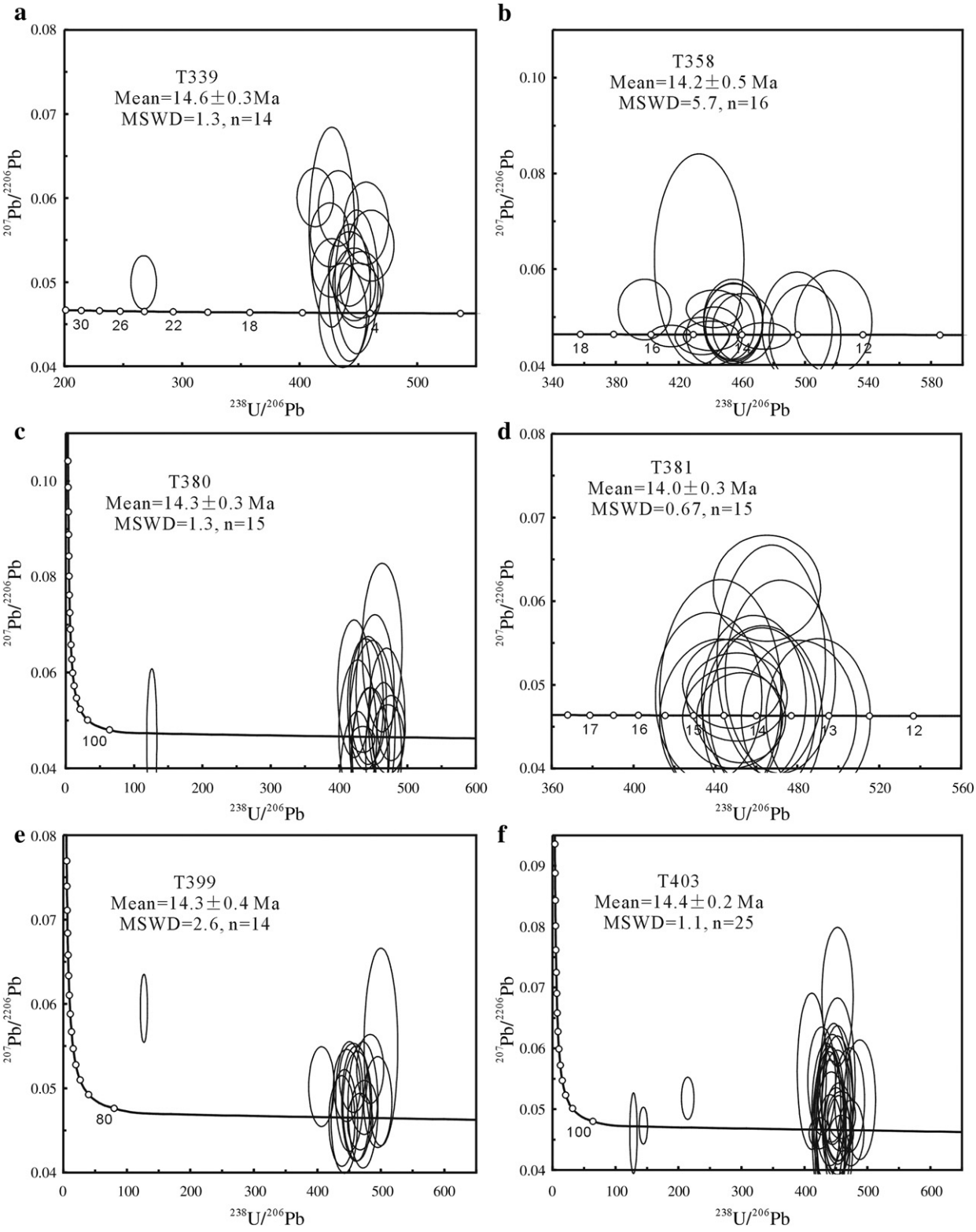

Fig. 3. Zircon U–Pb concordia diagrams. (a) Sample T399; (b) sample T358; (c) sample T380; (d) sample T381; (e) sample T399; (f) sample T403.

yield $^{206}Pb/^{238}U$ ages between 12.5±0.4 and 16.4±0.5 Ma, with a weighted mean of 14.3±0.5 Ma (2σ; MSWD=5.8) (Fig. 3b), representing the magma crystallization age. These zircons have U of 316–884 ppm, Th of 213–800 ppm and Th/U ratios of 0.67–1.22 (Table A).

Sample T403 from the NM granite was chosen for zircon U–Pb dating. Zircons from T403 are euhedral, colourless and transparent. They are long to short prismatic in shape, and show well-defined magmatic oscillatory zoning, as revealed by CL imaging (Fig. 2f). A few grains exhibit core-rim structure (Fig. 2f). Twenty-one zircon crystals with good magma oscillatory zoning were dated. They yield $^{206}Pb/^{238}U$ ages between 13.2±0.5 and 15.6±0.6 Ma, with a weighted mean of 14.4±0.2 Ma (2σ; MSWD=1.2) (Fig. 3f), which is interpreted as the magma crystallization age of the NM granite. In addition,

three analyses on the inherited cores give $^{206}Pb/^{238}U$ ages of 30.0 ± 0.9, 45.0 ± 1.0 and 50.0 ± 1.0 Ma, respectively. All zircons have U of 71.2–3832 ppm, Th of 130–4239 ppm and Th/U ratios of 0.35–2.09 (Table A).

Sample T399 was collected from the NM porphyry that intrudes the NM granite (Fig. 1b). Zircons in this sample display short to long prismatic, transparent and colourless grains. They have lengths of ~100 to ~150 μm and length/width ratios from 2:1 to 3:1. CL images show most zircons have magmatic oscillatory zoning and a few grains have core-rim structure (Fig. 2e). Fourteen zircon crystals with good magma oscillatory zoning were dated. They yield $^{206}Pb/^{238}U$ ages between 12.9 ± 0.5 and 15.8 ± 0.5 Ma, with a weighted mean of 14.0 ± 0.4 Ma (2σ; MSWD = 2.6) (Fig. 3e), representing the magma crystallization age. One analysis on the core gives a ~51 Ma inherited age. All zircons have U of 590–3985 ppm, Th of 355–1674 ppm and Th/U ratios of 0.33–1.09 (Table A).

Our zircon U–Pb dating shows that both the NM and PG granitoids and their associated porphyries have coeval magma crystallization ages around 14 Ma, which lie in the period (26–10 Ma) of the previously studied Gangdese high Sr/Y rocks (Chung et al., 2003; Hou et al., 2004; Gao et al., 2007).

4.2. Major and trace elements

Major and trace element data of all samples are given in Table 1.

The PG granodiorites display SiO_2 = 67.6–68.6%, Al_2O_3 = 15.5–15.9%, MgO = 1.11–1.37% and K_2O = 3.67–3.86%, with K_2O/Na_2O = 0.91–0.92. They have Mg# (Mg-numbers) ranging from 46 to 47 and

Table 1
Major (wt.%) and trace element (ppm) data for the PG and NM granitoids and their associated porphyries.

Sample	T339	T358	T379	T380	T381	T399	T400	T401	T402	T403	T404
	CJP	TGP	PG	PG	PG	NMP	NMP	NM	NM	NM	NM
SiO_2	69.25	66.09	67.63	68.44	68.61	67.95	67.93	69.75	71.50	69.68	72.09
TiO_2	0.45	0.41	0.38	0.33	0.36	0.42	0.46	0.33	0.33	0.31	0.33
Al_2O_3	15.21	15.37	15.53	15.90	15.64	15.44	15.34	15.01	14.03	14.93	13.80
$TFe_2O_3^*$	2.64	2.55	3.12	2.59	2.72	2.39	2.55	2.01	2.06	1.80	1.82
MnO	0.02	0.08	0.05	0.05	0.05	0.03	0.04	0.03	0.04	0.04	0.03
MgO	1.40	1.00	1.37	1.11	1.15	1.00	1.15	0.78	0.91	0.85	0.75
CaO	2.13	2.79	3.04	2.72	2.69	2.45	2.22	2.24	2.15	1.89	1.90
Na_2O	3.80	4.11	4.03	4.18	4.03	4.61	4.60	4.23	4.32	4.15	4.34
K_2O	4.00	3.59	3.67	3.86	3.72	4.21	4.11	4.82	4.00	5.56	4.21
P_2O_5	0.18	0.17	0.19	0.15	0.15	0.14	0.16	0.11	0.16	0.13	0.13
Lost	0.61	3.38	0.52	0.27	0.49	0.96	1.03	0.29	0.20	0.29	0.27
Total	99.69	99.54	99.53	99.60	99.61	99.60	99.59	99.60	99.70	99.63	99.67
K_2O/Na_2O	1.05	0.87	0.91	0.92	0.92	0.91	0.89	1.14	0.93	1.34	0.97
Mg#	51	44	47	46	46	45	47	43	47	48	45
A/CNK	1.05	0.98	0.96	0.99	1.01	0.93	0.96	0.92	0.91	0.92	0.91
Sc	5.34	4.27	5.44	4.46	4.52	3.91	4.21	3.44	3.66	3.17	3.49
V	52.7	47.5	58.8	45.0	48.3	47.7	52.0	36.4	36.1	33.0	33.7
Cr	18.6	11.2	23.5	15.2	14.1	8.90	10.5	6.79	17.1	13.8	10.1
Co	134	65.2	118	158	146	5.92	6.63	3.68	4.90	4.45	4.05
Ni	10.7	7.31	10.4	8.02	7.70	7.94	9.23	5.31	8.73	7.90	6.08
Cu	365	13.4	7.00	14.2	4.94	4.50	30.0	2.56	16.1	11.9	31.2
Zn	23.0	91.1	41.1	42.2	47.1	49.0	47.6	29.6	44.0	38.1	44.5
Ga	18.4	19.4	19.8	19.1	19.8	22.2	21.9	21.1	20.3	20.0	20.5
Rb	201	145	153	158	162	204	187	187	302	372	270
Sr	726	673	766	814	724	713	683	583	469	628	582
Y	8.29	6.69	8.42	6.20	7.17	7.99	10.4	7.75	7.41	7.12	7.08
Zr	84.1	103	90.8	73.9	110	94.9	122	107	99.9	88.3	116
Nb	7.52	6.25	7.83	5.78	6.91	7.92	7.83	8.94	10.8	10.2	8.54
Ba	889	855	845	1042	800	825	773	794	347	1146	672
La	28.6	28.4	32.9	24.6	29.6	35.9	39.9	35.5	32.0	34.2	45.4
Ce	62.4	60.6	68.9	52.3	60.2	70.5	78.7	71.0	66.1	67.7	90.2
Pr	7.00	6.58	7.58	5.94	6.70	7.56	8.59	7.31	7.29	7.38	8.81
Nd	26.2	24.6	27.0	21.0	23.8	26.3	30.0	24.5	25.9	25.7	29.0
Sm	4.44	3.88	4.37	3.58	4.00	4.48	5.11	3.96	4.55	4.55	4.80
Eu	1.00	0.96	1.08	0.93	0.93	0.97	1.03	0.88	0.80	1.01	0.88
Gd	2.62	2.32	2.82	2.09	2.42	2.65	3.13	2.44	2.50	2.63	2.67
Tb	0.31	0.27	0.34	0.26	0.29	0.34	0.42	0.31	0.31	0.31	0.32
Dy	1.45	1.28	1.55	1.22	1.40	1.63	2.02	1.56	1.48	1.41	1.37
Ho	0.27	0.21	0.28	0.20	0.24	0.24	0.32	0.22	0.23	0.23	0.23
Er	0.68	0.59	0.77	0.59	0.62	0.78	0.92	0.75	0.74	0.69	0.68
Tm	0.11	0.098	0.10	0.073	0.092	0.087	0.13	0.090	0.087	0.087	0.083
Yb	0.65	0.50	0.59	0.48	0.54	0.76	0.86	0.70	0.69	0.66	0.57
Lu	0.11	0.084	0.10	0.082	0.086	0.10	0.12	0.095	0.10	0.092	0.085
Hf	2.85	3.10	2.77	2.14	3.28	2.84	3.38	3.19	3.25	2.79	3.33
Ta	0.71	0.53	0.67	0.55	0.60	0.67	0.62	0.84	0.88	0.82	0.66
Pb	24.3	43.2	33.5	37.0	39.9	31.9	36.3	31.0	55.4	58.3	52.9
Th	27.2	21.6	31.9	22.6	29.1	21.9	21.9	26.8	51.7	44.9	29.5
U	5.34	4.62	6.19	2.66	5.13	4.31	5.39	4.04	12.7	12.7	5.13
Sr/Y	88	101	91	131	101	89	66	75	63	88	82
$(La/Yb)_N$	29.5	38.0	37.5	34.8	36.6	32.0	31.4	34.2	31.3	34.9	53.7
Nb/Ta	11	12	12	11	12	12	13	11	12	12	13
Eu/Eu*	0.82	0.91	0.88	0.95	0.85	0.79	0.73	0.81	0.66	0.82	0.69

Notes: CJP = Chongjiang porphyry; TGP = Tinggong porphyry; PG = Pagu granodiorite; NMP = Nanmuqie porphyry; NM = Nanmuqie granite. Mg# = (MgO/(MgO + FeOt)) * 100. A/CNK = molar $Al_2O_3/(CaO + Na_2O + K_2O)$.

A/CNK values <1.01, indicating that they are metaluminous. The Chongjiang and Tinggong porphyries that intrude the PG granodiorite have similar major element compositions to their host rocks (Table 1). In diagram of K_2O versus SiO_2, both the granodiorites and porphyries lie within the high-K calc-alkaline field (Fig. 4). The PG granodiorites and porphyries have high Sr contents (673–814 ppm) and low HREE and Y contents (Yb: 0.48–0.65 ppm; Y: 6.2–8.4 ppm), yielding high Sr/Y ratios of 88–131. They show strongly fractionated REE patterns (Fig. 5a), with $(La/Yb)_N = 30–38$ and $Eu/Eu^* = 0.80–1.07$. In trace element spider diagram (Fig. 6), both the granodiorites and porphyries show negative Nb, Ta, P and Ti anomalies, and are relatively enriched in Rb, Th, U, K and Pb.

The NM granites display $SiO_2 = 69.7–72.1\%$, $Al_2O_3 = 13.8–15.0\%$, $MgO = 0.75–0.91\%$ and $K_2O = 4.00–5.56\%$, with $K_2O/Na_2O = 0.93–1.34$. They have Mg# ranging from 43 to 48 and A/CNK values <1.0, indicating that they are metaluminous. The NM porphyries intruding the NM granite have slightly lower SiO_2 (67.9–68.0%) and higher Al_2O_3 (15.3–15.4%) and MgO (1.00–1.15%) than their host rocks. However, they have K_2O contents, Mg# and A/CNK values similar to their host rocks. The granites and porphyries are high-K calc-alkaline and shoshonitic (Fig. 4). Like the PG granodiorite and its associated porphyries, the NM granite and NM porphyry also display high Sr (469–713 ppm) and low HREE and Y (Yb: 0.57–0.86 ppm; Y: 7.1–10.4 ppm), resulting in high Sr/Y ratios of 63–89. They also show strongly fractionated REE patterns (Fig. 5b), with $(La/Yb)_N = 31–54$ and $Eu/Eu^* = 0.52–0.80$. Their trace element spider diagram patterns are similar to the PG granodiorite and its associated porphyries (Fig. 6).

Above geochemical signatures of the PG granodiorites, NM granites and their associated porphyries are similar to those of reported Miocene "adakitic" porphyries occurring in the Lhasa terrane (Chung et al., 2003; Hou et al., 2004; Qu et al., 2004; Gao et al., 2007; Guo et al., 2007). As shown in Fig. 7, samples from the PG granodiorite, NM granite and their associated porphyries fall in the field of adakite.

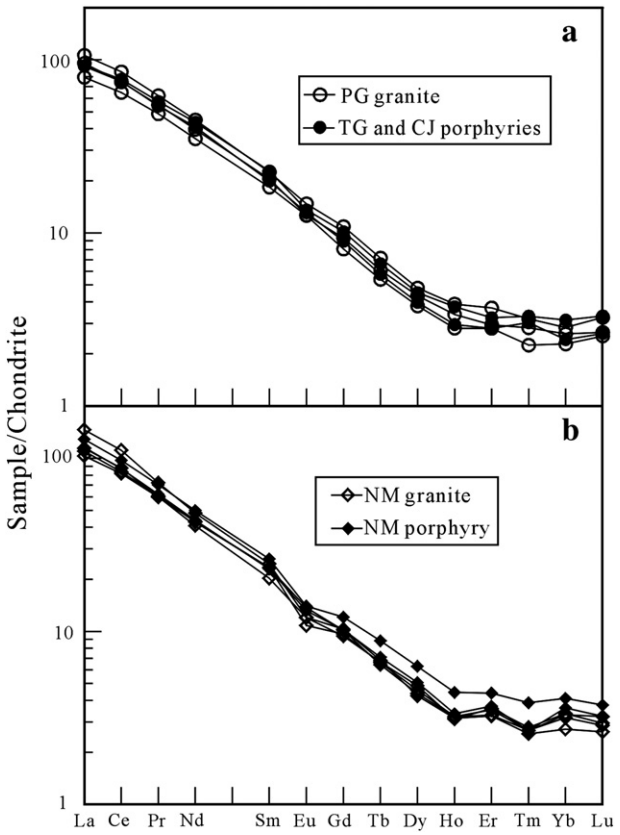

Fig. 5. Chondrite-normalized REE patterns. (a) PG granodiorite and its associated porphyries; (b) NM granite and its associated porphyry. Normalizing values from Boynton (1984).

4.3. Zircon Hf isotope

Zircon Lu–Hf isotope data are given in Table 2.

All Lu–Hf analyses were taken on the zircon grains in the same domains that the U–Pb ages were measured. Eleven analyses on zircons from the PG granodiorite T380 have $^{176}Hf/^{177}Hf$ ratios of 0.282786–0.282893, corresponding to $\varepsilon_{Hf}(t)$ values of +0.8 to +4.6 at $t = 14$ Ma. Twelve analyses on zircons from the NM granite T403 have slightly lower $^{176}Hf/^{177}Hf$ ratios of 0.282699–0.282783, corresponding to $\varepsilon_{Hf}(14\ Ma)$ values of −2.3 to +0.7. The porphyries show slightly higher $^{176}Hf/^{177}Hf$ ratios than their host granitoids. Twenty analyses on zircons from T339 (Chongjiang porphyry) and T358 (Tinggong porphyry) have $^{176}Hf/^{177}Hf$ ratios of 0.282835–0.282935, corresponding to $\varepsilon_{Hf}(14\ Ma)$ values of +2.5 to +6.1, with average $\varepsilon_{Hf}(t)$ values of $+4.9 \pm 0.9$ (MSWD = 2.1) for T339 and $+4.2 \pm 0.5$ (MSWD = 1.0) for T358. For the NM porphyry T399, twelve analyses

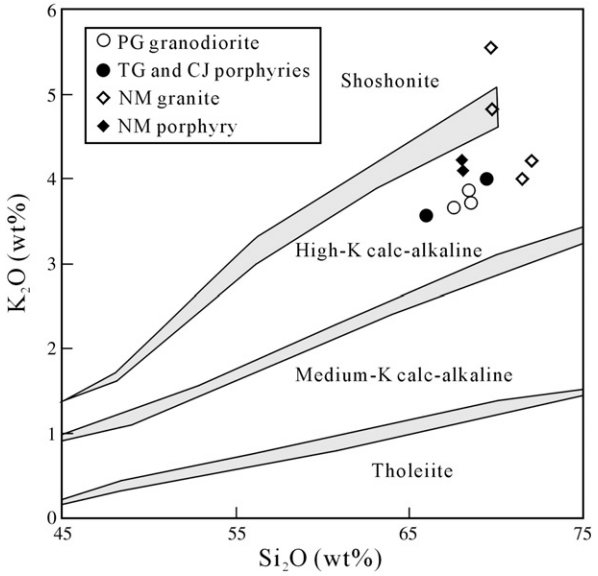

Fig. 4. Diagram of K_2O versus SiO_2. PG = Pagu, NM = Nanmuqie, CJ = Chongjiang, TG = Tinggong.

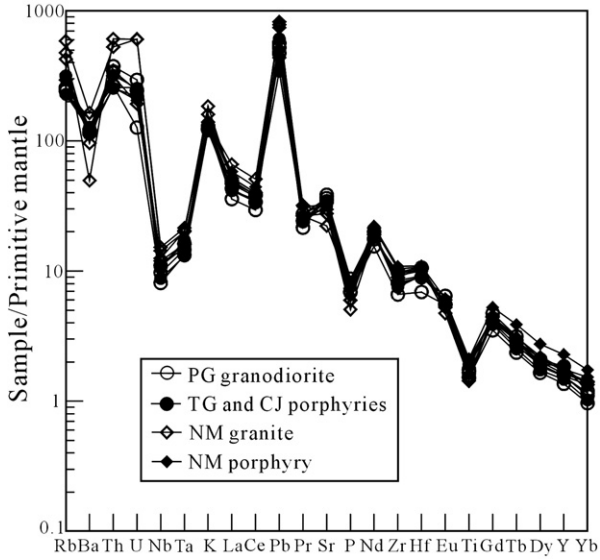

Fig. 6. Primitive mantle-normalized element spider diagram. Normalizing values from Sun and McDonough (1989).

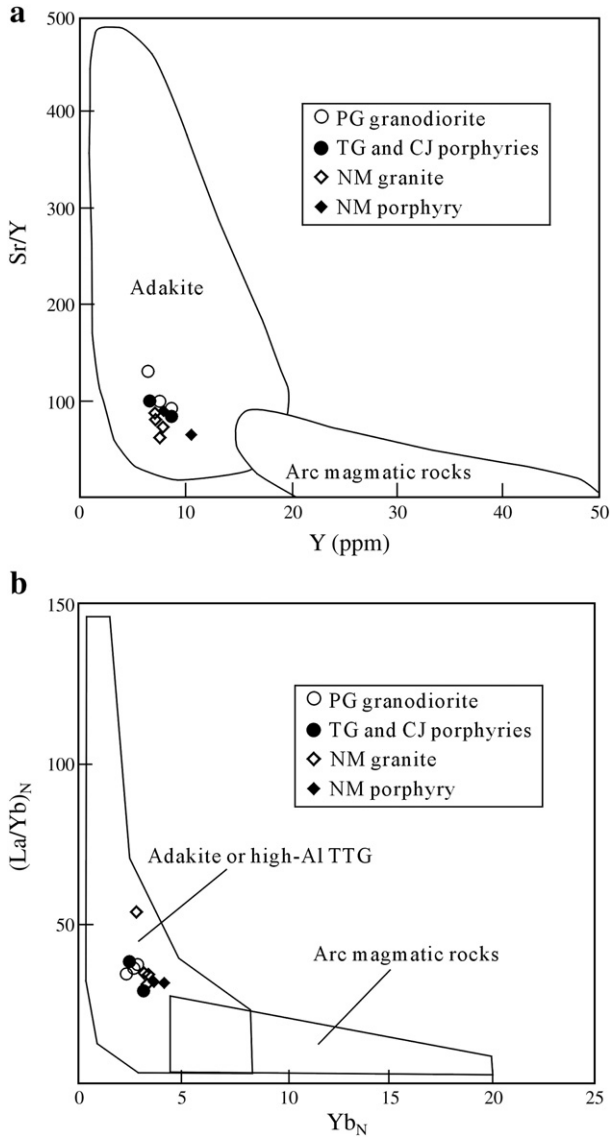

Fig. 7. (a) Diagram of Sr/Y versus Y; (b) diagram of $(La/Yb)_N$ versus Yb_N. Fields of adakite and arc magmatic rocks are from Defant et al. (2002).

show $^{176}Hf/^{177}Hf$ ratios of 0.282716–0.282828, corresponding to ε_{Hf} (14 Ma) values of −1.7 to +2.3.

4.4. Sr and Nd isotopes

Whole-rock Sr and Nd isotopic data are presented in Table 3.

For the PG granodiorite and NM granite, their initial $^{87}Sr/^{86}Sr$ (I_{Sr}) and $\varepsilon_{Nd}(t)$ values are calculated at their magma crystallization age of 14 Ma. The PG granodiorite has I_{Sr} values ranging from 0.70598 to 0.70621 and $\varepsilon_{Nd}(t)$ values ranging from −4.0 to −3.5, with mantle-depletion Nd model ages (T_{DM}) ranging from 0.95 to 0.99 Ga. The NM granite shows I_{Sr} values of 0.70642–0.70816 and $\varepsilon_{Nd}(t)$ values of −8.1 to −5.2, with T_{DM} = 1.13–1.23 Ga. The associated porphyries show similar Sr and Nd isotopic compositions to their host granitoids (Table 3), respectively.

5. Discussion

5.1. Previous models for the Gangdese high Sr/Y magma generation

Our study gives a new finding that the large-volume PG granodiorite and NM granite are geochemically similar to previously studied Gangdese "adakitic" porphyries in the Lhasa terrane (Chung et al., 2003; Hou et al., 2004; Qu et al., 2004; Gao et al., 2007; Guo et al., 2007). These high Sr/Y rocks form an E–W trending belt paralleling the Yarlung–Zangbo suture. Due to peculiar tectonic implication of the high Sr/Y rocks, exploring their magma source and petrogenesis will provide insights into tectonic evolution of the southern Tibet. So far, three models have been proposed for the origins of the Gangdese high Sr/Y porphyries and lavas. These include: (1) partial melting of the subducted Neotethyan oceanic crust, followed by interaction with an overlying mantle wedge (Qu et al., 2004); (2) partial melting of the thickened Lhasa lower crust (Chung et al., 2003; Hou et al., 2004); and (3) partial melting of an upper mantle source metasomatised by slab-derived melts (Gao et al., 2007). In the following, we will discuss the three models. None of these models adequately explains the petrogenesis of the Gangdese high Sr/Y rocks.

We firstly consider the possibility that the Gangdese high Sr/Y rocks originated by partial melting of subducted Neotethyan oceanic crust. Commonly, slab-derived high Sr/Y rocks (i.e., adakites) from modern arcs have relatively low K_2O contents and MORB-like Sr–Nd isotopic compositions (Kay, 1978; Defant and Drummond, 1990; Kay et al., 1993; Stern and Kilian, 1996). However, the Gangdese high Sr/Y rocks show abnormally high K_2O contents (high-K calc-alkaline realm) (Fig. 4), and relatively high initial $^{87}Sr/^{86}Sr$ (0.70470 to 0.70967) and low $\varepsilon_{Nd}(t)$ (+2.3 to −9.5) (Fig. 9) (this study; Miller et al., 1999; Hou et al., 2004; Guo et al., 2007), which are distinct from any slab-derived high Sr/Y rocks. On the other hand, the India–Eurasian continental collision initiated during the Paleocene (Beck et al., 1995; de Sigoyer et al., 2000; Leech et al., 2005; Yin, 2006), indicating that the oceanic crustal subduction underneath Asia had ceased at that time. Previous studies suggested that the Neotethyan slab is more likely to have been detached from the orogenic system and then to have been sunk into deep mantle in Eocene time (DeCelles et al., 2002; Kohn and Parkinson, 2002; Wen et al., 2008). This breakoff leads to the flare-up of magmatism in the Lhasa terrane (Wen et al., 2008). Therefore, partial melting of the previously subducted oceanic slab is not suitable to explain the magma generation of the Gangdese high Sr/Y rocks (26–10 Ma).

Chung et al. (2003) and Hou et al. (2004) suggested that these potassic high Sr/Y rocks were generated from partial melting of thickened Lhasa lower crust. Guo et al. (2007) further proposed that the magma source of these high Sr/Y rocks is a juvenile mafic-intermediate lower crust of the Lhasa terrane, which is similar to the Linzizong volcanic rocks (65–40 Ma) in chemical composition (Mo et al., 2007). If the model is correct, a thickened Lhasa crust (>50 km) prior to the high Sr/Y magmatism is necessary. Although geophysical data reveal that the Lhasa terrane has been thickened to approximately twice normal crustal thickness (Owens and Zandt, 1997; Molnar et al., 1998), whether it has achieved the thickness during early Miocene is still a matter of debate. For example, Nomade et al. (2004) suggested a much thinner crust of ~35 km in southern Tibet during Miocene volcanism. For this discussion, the composition of the Lhasa lower crust or crustal basement is a key. In the Lhasa terrane, the lower crust may have two types: (1) old crustal basement; and (2) juvenile mafic lower crust formed by mantle magma underplating during the Neotethyan oceanic subduction. Magma source of crust-derived granitoids is an alternative method to probe the crustal basement composition. As discussed in Zhang et al. (2007b), the Late-Triassic S- and I-type granitoids in the Lhasa terrane were derived from partial melting of sedimentary rocks and mafic rocks, respectively. Such magma sources could be indicative of the crustal basement composition in the Lhasa terrane. Although Sr–Nd isotopic data for the Late-Triassic granitoids are not available, obtained zircon Hf isotopic composition of the Triassic granitoids are distinct from that of the Gangdese high Sr/Y rocks (Fig. 8), indicating that the crustal basement, as revealed by the magma sources of the Triassic granitoids, cannot be taken as the magma source of the Gangdese high Sr/Y rocks. In the Lhasa terrane, exposed crustal basement is the Amdo orthogneiss

(531 Ma) with $^{87}Sr/^{86}Sr > 0.730$ and $\varepsilon_{Nd} < -10$ (Harris et al., 1988). Miller et al. (1999) assumed $^{87}Sr/^{86}Sr = 0.7100$ and $\varepsilon_{Nd} = -22$ for the Lhasa lower crust. Obviously, the exposed Lhasa crustal basement or the Lhasa lower crust alone cannot be taken as the magma source of the Gangdese high Sr/Y rocks (Fig. 9). The possibility that the Gangdese high Sr/Y magma was derived from partial melting of juvenile mafic lower crust can also be ruled out. Firstly, the Gangdese high Sr/Y rocks have Sr–Nd isotopic compositions partly overlapping with the Linzizong volcanic rocks (Fig. 9), which are considered to be the equivalent of the juvenile crust in the Lhasa terrane during the Eocene (Lee et al., 2007; Mo et al., 2007). So the partial melting of the juvenile crust cannot explain all the Gangdese high Sr/Y magma derivation. Secondly, Gao et al. (2008) suggested that the most primitive mafic rocks, ranging from picrite, basalt to basaltic andesite, in the Dazi area of the Lhasa terrane represent the underplating materials in the lower part of the Lhasa lower crust during the Eocene. These underplating materials are characterized by low K_2O (0.02–0.80%, mostly ~0.1%, Gao et al., 2008). It seems unlikely that partial melting of the underplated materials would generate the potassic rocks ($K_2O = 2.0$–8.6%, cluster around 4%) in the Lhasa terrane, given that the magma source possibly contains residual amphibole with a high partition coefficient for K.

Recently, Gao et al. (2007) suggested that the Gangdese high Sr/Y magma was derived from an upper mantle source metasomatised by slab-derived melts. If this was true, these high Sr/Y rocks would have relatively high Mg# and Cr and Ni contents. However, most high Sr/Y rocks in the Lhasa terrane have low Mg# (even <30), Cr and Ni contents and evolved Sr–Nd isotopic compositions (this study; Chung et al., 2003; Hou et al., 2004; Qu et al., 2004; Gao et al., 2007; Guo et al., 2007). This is inconsistent with the magma originating from partial melting of an upper mantle source. Additionally, low-degree hydrous melting of mantle peridotite can produce andesitic melts, but cannot generate voluminous felsic melts (Baker et al., 1995; Tatsumi, 2006; Mo et al., 2008). Therefore, the occurrence of large-volume PG and NM granitoids precludes the possibility that they were derived directly from partial melting of an upper mantle source metasomatised by slab-derived melts.

5.2. A possible model for the Gangdese high Sr/Y magma generation

Based on our geochemical data of the PG and NM granitoids and their associated porphyries, and previously published geochemical data of the high Sr/Y rocks in the Lhasa terrane (Chung et al., 2003; Hou et al., 2004; Qu et al., 2004; Gao et al., 2007; Guo et al., 2007), we propose an alternative model for the origin of the Gangdese high Sr/Y rocks. Geophysical data reveals that the Indian lithosphere was underthrusted beneath the Lhasa terrane, even as far north as the Bangong–Nujiang suture (Jin et al., 1996; Owens and Zandt, 1997; Rodgers and Schwartz, 1997; Tilmann et al., 2003; Schulte-Pelkum et al., 2005), following the India–Eurasian continental collision in the early Paleocene. Thus, it is possible that the Gangdese high Sr/Y magmas could be derived by partial melting of the northward subducted Indian mafic lower crust during the Miocene.

In order to test the possibility, we carry out a Sr–Nd–Hf isotopic compositional study for the mafic granulites in the eastern Himalayan syntaxis. The mafic granulites had experienced high-pressure metamorphism, resulting from continental subduction of the Indian plate (Zhong and Ding, 1996; Liu and Zhong, 1997; Ding et al., 2001; Geng et al., 2006; Liu et al., 2007a, 2007b; Zhang et al., 2007c). The mafic granulites, consisting of garnet, clinopyroxene, amphibole, quartz, rutile and titanite, occur as boudins in garnet-bearing gneiss. They represent the lower crustal composition of the northern Indian plate (Zhong and Ding, 1996; Geng et al., 2006).

Zircon Hf isotopic data of the mafic granulite in the eastern Himalayan syntaxis (Table 2) show that their $\varepsilon_{Hf}(14\ Ma)$ values (−2.5 to +4.8) overlap with those (−2.3 to +6.1) of the PG granodiorite, NM granite and their associated porphyries (Fig. 8), indicating that the mafic granulite could be taken as their magma source. Whole-rock Sr–Nd isotopic data of the mafic granulites (Table 3) show that they have $^{143}Nd/^{144}Nd$ ratios of 0.51258–0.51280 ($\varepsilon_{Nd}(14\ Ma) = -1.0$–+3.2), similar to the estimated ratios (0.5125–0.5127) of the Indian mafic lower crust (Hou et al., 2004). They have $^{87}Sr/^{86}Sr$ ratios of 0.70587 to 0.71114, which are higher than the estimated ratios (0.7044 to 0.7047) of the Indian mafic lower crust (Hou et al., 2004). Considering possible Sr–Nd mobility during metamorphism, we take the maximum $^{143}Nd/^{144}Nd$ ratio of 0.51280 and minimum $^{87}Sr/^{86}Sr$ ratio of 0.70440 as the Sr–Nd isotopic composition of the mafic granulite protolith. On $\varepsilon_{Nd}(t)$ versus I_{Sr} diagram (Fig. 9), the PG granodiorite, NM granite and their associated porphyries, together with previously studied high Sr/Y porphyries and lavas (Miller et al., 1999; Hou et al., 2004; Guo et al., 2007), fall in the field defined by the two-endmember mixing between the Indian mafic lower crust and the ultrapotassic lavas/the Lhasa lower crust, indicating that the Gangdese high Sr/Y magmas could be derived from partial melting of the Indian mafic lower crust, but contaminated by the ultrapotassic magma and/or the lower crustal materials in the Lhasa terrane during the high Sr/Y magma emplacement. The NM granite and its associated porphyry have higher initial $^{87}Sr/^{86}Sr$, lower $\varepsilon_{Nd}(t)$ and $\varepsilon_{Hf}(t)$ values than the PG granodiorite and its associated porphyries. This implies that the NM granite and its associated porphyry incorporate more of the ultrapotassic lava and/or the Lhasa lower crust components than the PG granodiorite and its associated porphyries.

According to the above discussion, we suggest that the Gangdese high Sr/Y rocks originated by partial melting of the subducted Indian mafic lower crust, with minor incorporation of the ultrapotassic lava and/or the Lhasa lower crust components. This is also supported by the following two lines of evidence. Firstly, the Gangdese high Sr/Y rocks spread along an E–W trending belt paralleling the Yarlung–Zangbo suture. The distribution pattern can be interpreted by the Indian continental deep subduction. Secondly, both Nb and Ta show similar geochemical behaviors, and thus the Nb/Ta ratio is hardly affected by magmatic processes such as fractional crystallization and partial melting (Jiang et al., 2006). The PG and NM granitoids as well as their porphyries have Nb/Ta ratios of 11–13, being slightly lower than but close to the mafic granulites (Nb/Ta = 13–14, author's unpublished data) in the eastern Himalayan syntaxis, consistent with the minor incorporation of the other components.

If the high Sr/Y rocks are derived directly from partial melting of mafic rocks, they should have relatively low K_2O contents, as demonstrated by experimental studies (Rapp and Waston, 1995). However, the high Sr/Y rocks in the Lhasa terrane have relatively high K_2O contents (3.6–5.6 wt.%), suggesting that pristine melts must have experienced a process elevating the K_2O contents. Note that the high Sr/Y rocks and the ultrapotassic rocks overlap spatially and temporally in the southern Lhasa terrane (Nomade et al., 2004). Therefore a binary mixing between pristine high Sr/Y melts and ultrapotassic melts seem to be a possible process that resulted in the high K. This mixing model is also consistent with the Sr–Nd data (Fig. 9).

5.3. Tectonic implications

Our geochemical study on the high Sr/Y rocks in the Lhasa terrane suggest that the magma originated from partial melting of the Indian mafic lower crust. That is to say, the Indian lithosphere has underthrusted beneath the southern Lhasa terrane during the early–middle Miocene, further validating previous geophysical interpretation (Jin et al., 1996; Owens and Zandt, 1997; Rodgers and Schwartz, 1997; Tilmann et al., 2003; Schulte-Pelkum et al., 2005).

According to the above discussion, we propose a tectonic model for the genesis of the high Sr/Y rocks in the Lhasa terrane (Fig. 10). The India–Asian collision initiated at the Paleocene (Beck et al., 1995; de Sigoyer et al., 2000; Mo et al., 2003; Leech et al., 2005; Yin, 2006), which caused the convergence rate to decrease abruptly

Table 2
Zircon Lu–Hf isotopic data.

Analysis	$^{176}Yb/^{177}Hf$	$^{176}Lu/^{177}Hf$	$^{176}Hf/^{177}Hf$	$\pm(2\sigma)$	ε_{Hf}(14 Ma)	$\pm$(2 s)	T_{DM1} (Ma)	$\pm(2\sigma)$	T_{DM2} (Ma)	$\pm(2\sigma)$	U–Pb spot
Chongjiang porphyry T339											
T339-01	0.025098	0.000794	0.282914	0.000024	5.3	0.8	477	68	754	109	339-2
T339-02	0.012454	0.000430	0.282923	0.000020	5.6	0.7	460	55	734	90	339-3
T339-03	0.014457	0.000498	0.282920	0.000028	5.5	1.0	465	79	740	127	339-8
T339-04	0.018975	0.000625	0.282885	0.000024	4.3	0.8	515	67	820	108	339-6
T339-05	0.013670	0.000467	0.282835	0.000024	2.5	0.8	583	67	932	108	339-5
T339-06	0.023589	0.000774	0.282912	0.000024	5.3	0.8	479	68	759	109	339-4
T339-07	0.019966	0.000667	0.282935	0.000022	6.1	0.8	446	62	707	100	339-12
T339-08	0.017414	0.000535	0.282853	0.000026	3.2	0.9	559	73	892	117	339-13
T339-09	0.021801	0.000710	0.282919	0.000020	5.5	0.7	469	56	743	90	339-14
Tinggong porphyry T358											
T358-01	0.019714	0.000586	0.282864	0.000022	3.6	0.8	545	62	868	99	358-1
T358-02	0.034948	0.000975	0.282890	0.000032	4.5	1.1	513	91	809	145	358-2
T358-03	0.027293	0.000787	0.282875	0.000032	3.9	1.1	532	90	843	145	358-4
T358-04	0.019948	0.000641	0.282886	0.000022	4.3	0.8	515	62	818	99	358-3
T358-05	0.019289	0.000616	0.282855	0.000026	3.2	0.9	558	73	888	117	358-6
T358-06	0.019146	0.000599	0.282887	0.000024	4.4	0.8	513	67	816	108	358-12
T358-07	0.019625	0.000646	0.282935	0.000020	6.1	0.7	446	56	707	91	358-10
T358-08	0.015581	0.000502	0.282878	0.000022	4.0	0.8	524	62	836	99	358-9
T358-09	0.020504	0.000620	0.282873	0.000018	3.9	0.6	533	51	847	82	358-8
T358-10	0.019547	0.000657	0.282881	0.000018	4.2	0.6	522	50	829	80	358-15
T358-11	0.028134	0.000752	0.282868	0.000026	3.7	0.9	541	73	859	117	358-16
Pagu granodiorite T380											
T380-01	0.014797	0.000506	0.282893	0.000028	4.6	1.0	503	78	802	127	380-1
T380-02	0.020763	0.000704	0.282826	0.000056	2.2	2.0	600	158	954	253	380-2
T380-03	0.021125	0.000671	0.282849	0.000034	3.0	1.2	567	96	902	154	380-4
T380-04	0.021533	0.000681	0.282849	0.000032	3.0	1.1	567	90	902	144	380-3
T380-05	0.016983	0.000570	0.282813	0.000024	1.7	0.8	616	67	983	108	380-9
T380-06	0.018893	0.000575	0.282803	0.000038	1.4	1.3	630	106	1006	171	380-8
T380-07	0.016514	0.000551	0.282878	0.000022	4.0	0.8	525	62	836	99	380-7
T380-08	0.014328	0.000490	0.282854	0.000044	3.2	1.6	558	123	891	199	380-6
T380-09	0.015110	0.000508	0.282786	0.000046	0.8	1.6	653	129	1044	207	380-14
T380-10	0.017702	0.000620	0.282839	0.000024	2.7	0.8	581	67	925	108	380-13
T380-11	0.018943	0.000650	0.282847	0.000030	2.9	1.1	570	84	906	135	380-12
Nanmuqie porphyry 399											
T399-01	0.078985	0.002005	0.282787	0.000046	0.8	1.6	677	134	1041	207	399-1
T399-02	0.025783	0.000776	0.282787	0.000042	0.8	1.5	655	118	1041	189	399-3
T399-03	0.035452	0.001029	0.282753	0.000034	−0.4	1.2	708	96	1117	153	399-5
T399-04	0.035275	0.000898	0.282828	0.000030	2.3	1.1	600	85	948	135	399-9
T399-05	0.028573	0.000864	0.282807	0.000034	1.5	1.2	629	96	996	153	399-8
T399-06	0.028829	0.000852	0.282805	0.000019	1.5	0.7	631	53	1000	84	399-10
T399-07	0.033996	0.000935	0.282761	0.000048	−0.1	1.7	695	136	1099	216	399-6
T399-08	0.026749	0.000760	0.282716	0.000028	−1.7	1.0	755	79	1201	126	399-8
T399-09	0.032028	0.000911	0.282719	0.000022	−1.6	0.8	754	62	1194	99	399-13
T399-10	0.026994	0.000795	0.282783	0.000024	0.7	0.8	661	68	1050	108	399-15
T399-11	0.037409	0.001048	0.282742	0.000022	−0.8	0.8	724	62	1142	99	399-14
T399-12	0.058190	0.001543	0.282786	0.000032	0.8	1.1	670	92	1043	144	399-11
Nanmuqie granite T403											
T403-01	0.061403	0.001855	0.282721	0.000020	−1.5	0.7	771	57	1191	89	403-1
T403-02	0.026553	0.000829	0.282783	0.000028	0.7	1.0	663	79	1051	126	403-5
T403-03	0.022083	0.000762	0.282743	0.000026	−0.7	0.9	718	73	1141	117	403-4
T403-04	0.022166	0.000639	0.282774	0.000044	0.4	1.6	672	123	1071	198	403-3
T403-05	0.054950	0.001482	0.282762	0.000034	−0.1	1.2	704	97	1098	153	403-2
T403-06	0.021876	0.000661	0.282783	0.000024	0.7	0.8	660	67	1051	108	403-9
T403-07	0.010923	0.000362	0.282745	0.000030	−0.7	1.1	707	83	1136	135	403-7
T403-08	0.015575	0.000542	0.282765	0.000022	0.0	0.8	683	62	1091	99	403-14
T403-09	0.032899	0.000925	0.282699	0.000022	−2.3	0.8	783	62	1240	99	403-16
T403-10	0.013470	0.000444	0.282721	0.000020	−1.5	0.7	742	56	1190	90	403-17
T403-11	0.023876	0.000752	0.282728	0.000020	−1.3	0.7	739	56	1175	90	403-20
T403-12	0.022279	0.000646	0.282762	0.000030	−0.1	1.1	689	84	1098	135	403-19
Mafic granulite T605 from eastern Himalayan syntaxis											
T605-04	0.001795	0.000059	0.282804	0.000019	1.4	0.7	621	54	997	88	
T605-07	0.002404	0.000075	0.282782	0.000021	0.7	0.8	650	59	1045	97	
T605-08	0.003444	0.000112	0.282748	0.000020	−0.5	0.7	699	56	1123	91	
T605-09	0.001474	0.000046	0.282772	0.000017	0.3	0.6	663	47	1067	77	
T605-10	0.003804	0.000122	0.282749	0.000021	−0.5	0.7	697	58	1120	94	
T605-12	0.003379	0.000116	0.282710	0.000020	−1.9	0.7	751	55	1208	90	
T605-13	0.001891	0.000063	0.282761	0.000018	−0.1	0.6	680	49	1093	81	
T605-15	0.001632	0.000057	0.282883	0.000022	4.2	0.8	510	61	817	99	

Table 2 (*continued*)

Analysis	$^{176}Yb/^{177}Hf$	$^{176}Lu/^{177}Hf$	$^{176}Hf/^{177}Hf$	$\pm(2\sigma)$	ε_{Hf}(14 Ma)	$\pm$(2 s)	T_{DM1} (Ma)	$\pm(2\sigma)$	T_{DM2} (Ma)	$\pm(2\sigma)$	U–Pb spot
Mafic granulite T605 from eastern Himalayan syntaxis											
T605-16	0.000481	0.000013	0.282872	0.000017	3.8	0.6	525	46	843	75	
T605-18	0.003090	0.000098	0.282692	0.000021	−2.5	0.8	776	59	1249	96	
T605-19	0.004267	0.000139	0.282716	0.000019	−1.7	0.7	743	53	1194	86	
T605-20	0.003467	0.000115	0.282762	0.000021	−0.1	0.7	679	58	1092	94	
T605-21	0.000490	0.000013	0.282900	0.000020	4.8	0.7	487	54	781	89	
T605-23	0.003539	0.000115	0.282764	0.000019	0.0	0.7	676	53	1086	87	
T605-25	0.003259	0.000110	0.282743	0.000019	−0.7	0.7	705	52	1133	85	
T605-26	0.000538	0.000017	0.282837	0.000020	2.6	0.7	574	56	922	91	
T605-27	0.000564	0.000019	0.282899	0.000017	4.8	0.6	489	46	783	75	
T605-05	0.001441	0.000041	0.282857	0.000018	3.3	0.6	546	49	873	80	
T605-14	0.000831	0.000025	0.282898	0.000018	4.8	0.6	489	49	781	80	

Notes: $\varepsilon_{Hf}(t) = 10{,}000\{[(^{176}Hf/^{177}Hf)_s - (^{176}Lu/^{177}Hf)_s \times (e^{\lambda t} - 1)]/[(^{176}Hf/^{177}Hf)_{CHUR,0} - (^{176}Lu/^{177}Hf)_{CHUR} \times (e^{\lambda t} - 1)] - 1\}$; $T_{DM1} = 1/\lambda \times \ln\{1 + [((^{176}Hf/^{177}Hf)_s - (^{176}Hf/^{177}Hf)_{DM}]/[(^{176}Lu/^{177}Hf)_s - (^{176}Lu/^{177}Hf)_{DM}]\}$; $T_{DM2} = T_{DM1} - (T_{DM1} - t)[(f_{cc} - f_s)/(f_{cc} - f_{DM})]$, where f_{cc}, f_s and f_{DM} are the $f_{Lu/Hf}$ values of continental crust, sample and depleted mantle, respectively.

around 55 Ma (Klootwijk et al., 1992; Acton, 1999). Wen et al. (2008) argued that the Neotethyan slab breakoff (i.e. detachment of the subducted Neotethyan oceanic slab from the adherent but more buoyant Indian continental lithosphere) took place at around 50 Ma, which produce extensive magmatism in the Lhasa terrane, i.e., the Linzizong volcanic rocks and the Gangdese batholith. After that, the Indian continental margin began to be subducted beneath the Lhasa terrane with a slow subduction velocity and low subduction angle (Guillot et al., 2008), which squeezed out the Asian lithosphere and terminated the Gangdese magmatism between ~40 and 25 Ma in the southern Tibet (Maheo et al., 2002; Chung et al., 2005). By ~25 Ma, the subducted felsic part was detached from the subjacent mafic part and lithosphere mantle of the Indian plate (Li, 2004). The above felsic part was exhumed due to the buoyancy. This felsic part is equivalent to the Great Himalayan Sequence in the Himalayan terrane. The residual mafic part and lithosphere mantle became steeper from low-angle underthrusting to high-angle underthrusting, even forming a sub-vertical lithosphere slab. A consequence of this downwelling would be a deficit of asthenosphere, which should be balanced by an upwelling counterflow, and thus warm both the Asian mantle and the Indian mafic lower crust. It would induce partial melting of the Indian mafic lower crust to produce the pristine high Sr/Y melt. During the magma migration and emplacement, the magma may incorporate the ultrapotassic magmas and/or the Lhasa lower crust materials.

The high Sr/Y PG granodiorite and NM granite were intruded by the high Sr/Y porphyries, respectively. Generally, the granitic magma crystallizes at middle-crust depth, whereas the porphyry magma was intruded at upper-crust depth. Our geochronological study reveals that the PG granodiorite and NM granite formed at ~14 Ma that is indistinguishable from their associated porphyries in age. A probable interpretation is that the magmas of the PG granodiorite and NM granite crystallized at middle-crust depth, followed by a fast uplift to upper crust, and were then intruded by the high Sr/Y porphyries, indicating a fast crustal uplift process around 14 Ma. This is consistent with the previous conclusion that the fast crustal uplift in the southern Tibet occurred in the Miocene (Coleman and Hodges, 1995; Spicer et al., 2003). Therefore, the association of the coeval high Sr/Y granitoids and porphyries can be taken as an indicator of fast crustal uplift in the southern Tibet.

6. Conclusions

The large-volume PG and NM granitoids are firstly identified to be high Sr/Y intrusive rocks. Together with previously reported high Sr/Y rocks, they form an E–W trending belt paralleling the Yarlung–Zangbo suture, south Tibet. Geochemical and Sr–Nd–Hf isotopic data reveal that the high Sr/Y magmas in the Lhasa terrane could be derived from partial melting of subducted Indian mafic lower crust with minor incorporation of the ultrapotassic lava and/or the Lhasa lower crust components. This is significantly different from previous magma generation model of the high Sr/Y rocks in the Lhasa terrane. Our model suggests that the Indian continental crust was subducted beneath the southern Lhasa terrane

Table 3
Data for whole-rock Sr and Nd isotopes.

Sample		$^{87}Rb/^{86}Sr$	$^{87}Sr/^{86}Sr$	$\pm 2\sigma$	I_{Sr}(14 Ma)	$^{147}Sm/^{144}Nd$	$^{143}Nd/^{144}Nd$	$\pm 2\sigma$	ε_{Nd}(14 Ma)	T_{DM} (Ga)
PG granodiorite, NM granite and their associated porphyry										
T358	TGP	0.400	0.70570	3	0.70562	0.098	0.512505	3	−2.4	0.85
T379	PG	0.581	0.70633	5	0.70621	0.098	0.512424	3	−4.0	0.96
T380	PG	0.564	0.70612	3	0.70601	0.103	0.512436	2	−3.8	0.99
T381	PG	0.651	0.70611	3	0.70598	0.102	0.512449	2	−3.5	0.95
T399	NMP	0.829	0.70693	3	0.70677	0.103	0.512330	2	−5.8	1.13
T400	NMP	0.795	0.70699	3	0.70684	0.103	0.512347	2	−5.5	1.11
T401	NM	0.930	0.70835	3	0.70816	0.098	0.512215	2	−8.1	1.23
T403	NM	1.716	0.70677	3	0.70642	0.107	0.512363	2	−5.2	1.13
T404	NM	1.343	0.70784	3	0.70757	0.100	0.512251	1	−7.4	1.20
Mafic granulite from eastern Himalayan syntaxis										
T604	MG	0.236	0.70734	7	0.70730	0.187	0.512743	1	2.1	2.29
T605	MG	0.290	0.70587	6	0.70581	0.184	0.512769	1	2.6	1.98
T606	MG	0.202	0.70780	5	0.70776	0.185	0.512803	1	3.2	1.85
T607	MG	1.497	0.71114	4	0.71084	0.184	0.512584	1	−1.0	2.91
T608	MG	0.276	0.70913	4	0.709073	0.176	0.512672	2	0.7	1.94

Notes: $^{87}Rb/^{86}Sr$ and $^{147}Sm/^{144}Nd$ ratios are calculated using Rb, Sr, Sm and Nd contents (Table 2), measured by ICP-MS; $\varepsilon_{Nd}(t)$ values are calculated using present-day $(^{147}Sm/^{144}Nd)_{CHUR} = 0.1967$ and $(^{143}Nd/^{144}Nd)_{CHUR} = 0.512638$; T_{DM} values are calculated using present-day $(^{147}Sm/^{144}Nd)_{DM} = 0.2137$ and $(^{143}Nd/^{144}Nd)_{DM} = 0.51315$. TGP = Tinggong porphyry; PG = Pagu granodiorite; NMP = Nanmuqie porphyry; NM = Nanmuqie granite; MG = mafic granulite.

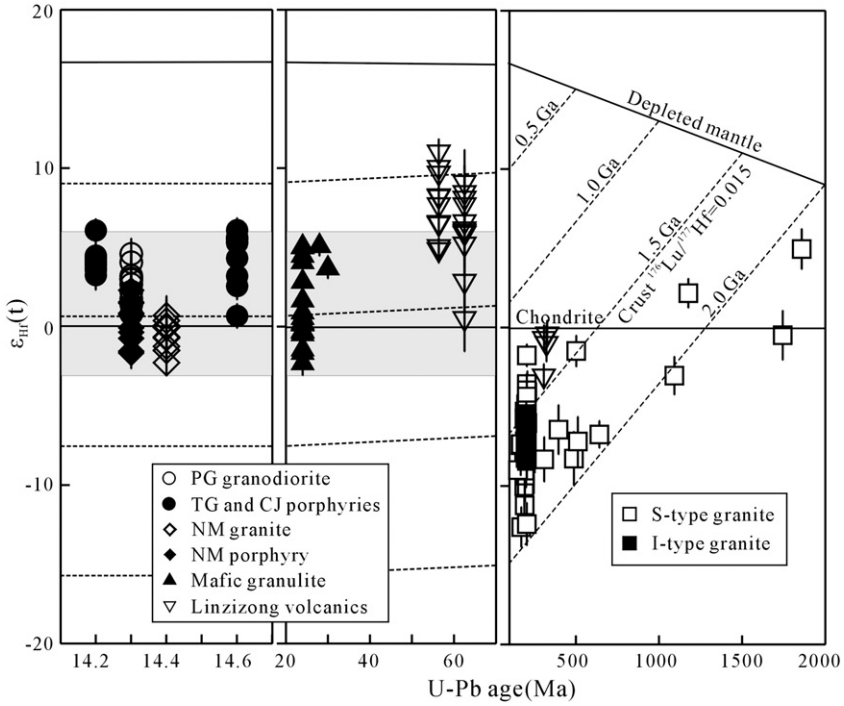

Fig. 8. Plot of zircon $\varepsilon_{Hf}(t)$ versus zircon $^{206}Pb/^{238}U$ age. $\varepsilon_{Hf}(t)$ values of the Linzizong volcanic rocks were plotted for comparison. Grey shaded area shows the Hf isotopic evolutional trend of the analyzed zircons from the mafic granulite in the eastern Himalayan syntaxis. Data source: (1) S-type granites from Chu et al. (2006) and Zhang et al. (2007b); (2) I-type granite from Zhang et al. (2007b); and (3) Linzizong volcanic rocks from Lee et al. (2007).

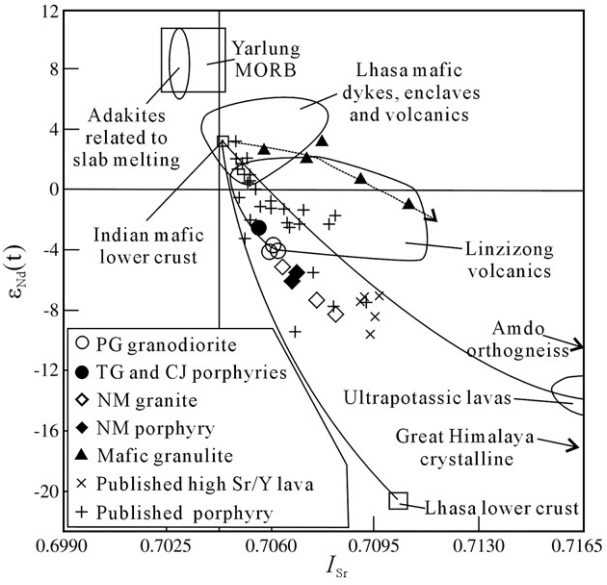

Fig. 9. $\varepsilon_{Nd}(t)$ versus I_{Sr} diagram of the PG and NM granitoids and their associated porphyries. The previous results on the Gangdese high Sr/Y porphyries and lavas were plotted for comparison (Miller et al., 1999; Hou et al., 2004; Guo et al., 2007). Data of the Lhasa lower crust ($^{87}Sr/^{86}Sr = 0.7100$, $^{143}Nd/^{144}Nd = 0.5115$) and the Miocene ultrapotassic lavas are from Miller et al. (1999). Adakites from slab melting are from the Adak Island, Cook Island and Cerro Pampa (Kay, 1978; Kay et al., 1993; Stern and Kilian, 1996). Data for Amdo orthogneiss (Harris et al., 1988) and Great Himalaya crystalline rocks (author's unpublished data) are also plotted for comparison. Field of Linzizong volcanic rocks is from Yue and Ding (2006), Mo et al. (2007) and Mo et al. (2008), and field of Lhasa mafic dykes, enclaves and volcanics from Jiang et al. (1999), Yue and Ding (2006), Mo et al. (2007) and Gao et al. (2008). The Lhasa mafic dykes, enclaves and volcanics are regarded as the underplating materials in the lower part of the Lhasa lower crust during the Eocene (Gao et al., 2008). The dotted line shows possible Sr–Nd movement during retrograde metamorphism.

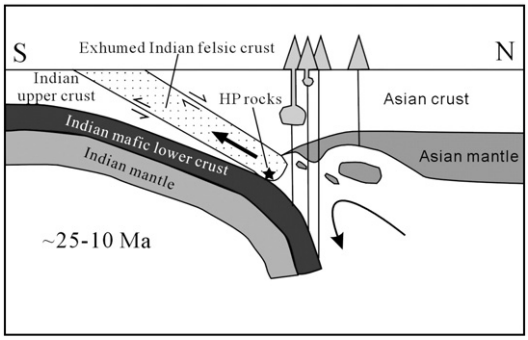

Fig. 10. A proposed model for petrogenesis of the high Sr/Y rocks in the Lhasa terrane, south Tibet. HP = high pressure.

during the early–middle Miocene. The association of the coeval high Sr/Y granitoids and porphyries may suggest that the fast crustal uplift in the southern Tibet occurred at ~14 Ma.

Acknowledgements

This research was supported by the Natural Science Foundation of China (Grant 40773019 and 40821061) and by the Ministry of Education of China and the State Administration of Foreign Expert Affairs of China (Grant B07039) and by Opening Foundation of the State Key Laboratory of Geological Process and Mineral Resource. We thank Prof. Min Sun, an anonymous reviewer and Editor Nelson Eby for the constructive comments that greatly improved this manuscript.

Appendix A. Supplementary data

Supplementary data associated with this article can be found, in the online version, at doi:10.1016/j.lithos.2009.09.005.

References

Acton, G., 1999. Apparent polar wander of India since the Cretaceous with implications for regional tectonics and true polar wander. Memoir-Geological Society of India 44, 129–175.

An, Z.S., Kutzbach, J.E., Prell, W.L., Porter, S.C., 2001. Evolution of Asian monsoons and phased uplift of the Himalayan Tibetan plateau since Late Miocene times. Nature 411, 62–66.

Andersen, T., 2002. Correction of common lead in U–Pb analyses that do not report ^{204}Pb. Chemical Geology 192 (1–2), 59–79.

Baker, M., Hirschmann, M., Ghiorso, M., Stolper, E., 1995. Compositions of near-solidus peridotite melts from experiments and thermodynamic calculations. Nature 375, 308–311.

Beck, R.A., Burbank, D.W., Sercombe, W.J., Riley, G.W., Barndt, J.K., Berry, J.R., Afzal, J., Khan, A.M., Jurgen, H., Metje, J., Cheema, A., Shafique, N.A., Lawrence, R.D., Khan, M.A., 1995. Stratigraphic evidence for an early collision between northwest India and Asia. Nature 373, 55–58.

Blichert-Toft, J., Albarede, F., 1997. The Lu–Hf isotope geochemistry of chondrites and the evolution of the mantle–crust system. Earth and Planetary Science Letters 148, 243–258.

Blisniuk, P.M., Hacker, B.R., Glodny, J., Ratschbacher, L., Bi, S., Wu, Z.H., McWilliams, M.O., Calvert, A., 2001. Normal faulting in central Tibet since at least 13.5 Myr ago. Nature 412, 628–632.

Boynton, W., 1984. Geochemistry of the rare earth elements: meteorite studies. In: Henderson, P. (Ed.), Rare Earth Element Geochemistry, pp. 63–114.

Chu, M.F., Chung, S.L., Song, B., Liu, D.Y., O'Reilly, S.Y., Pearson, N.J., Ji, J.Q., Wen, D.J., 2006. Zircon U–Pb and Hf isotope constraints on the Mesozoic tectonics and crustal evolution of southern Tibet. Geology 34 (9), 745–748.

Chung, S.L., Liu, D.Y., Ji, J.Q., Chu, M.F., Lee, H.Y., Wen, D.J., Lo, C.H., Lee, T.Y., Qian, Q., Zhang, Q., 2003. Adakites from continental collision zones: melting of thickened lower crust beneath southern Tibet. Geology 31 (11), 1021–1024.

Chung, S.L., Chu, M.F., Zhang, Y.Q., Xie, Y.W., Lo, C.H., Lee, T.Y., Lan, C.Y., Li, X.H., Zhang, Q., Wang, Y.Z., 2005. Tibetan tectonic evolution inferred from spatial and temporal variations in post-collisional magmatism. Earth Science Reviews 68, 173–196.

Coleman, M., Hodges, K., 1995. Evidence for Tibetan plateau uplift before 14 Myr ago from a new minimum age for east–west extension. Nature 374, 49–52.

Corfu, F., Hanchar, J., Hoskin, P., Kinny, P., 2003. Atlas of zircon textures. Reviews in Mineralogy and Geochemistry 53 (1), 469–500.

de Sigoyer, J., Chavagnac, V., Blichert-Toft, J., Villa, I.M., Luais, B., Guillot, S., Cosca, M., Mascle, G., 2000. Dating the Indian continental subduction and collisional thickening in the northwest Himalaya: multichronology of the Tso Morari eclogites. Geology 28 (6), 487–490.

DeCelles, P.G., Robinson, D.M., Zandt, G., 2002. Implications of shortening in the Himalayan fold-thrust belt for uplift of the Tibetan Plateau. Tectonics 21 (1062). doi:10.1029/2001TC001322.

Defant, M., Drummond, M., 1990. Derivation of some modern arc magmas by melting of young subducted lithosphere. Nature 347, 662–665.

Defant, M.J., Xu, J.F., Kepezhinskas, P., Wang, Q., Zhang, Q., Xiao, L., 2002. Adakites: some variations on a theme. Acta Petrologica Sinica 18, 129–142.

Derry, L.A., France-Lanord, C., 1996. Neogene Himalayan weathering history and river ^{87}Sr/^{86}Sr: impact on the marine Sr record. Earth and Planetary Science Letters 142 (1–2), 59–74.

Ding, L., Zhong, D.L., Yin, A., Kapp, P., Harrison, T.M., 2001. Cenozoic structural and metamorphic evolution of the eastern Himalayan syntaxis (Namche Barwa). Earth and Planetary Science Letters 192 (3), 423–438.

Ding, L., Kapp, P., Zhong, D.L., Deng, W.M., 2003. Cenozoic volcanism in Tibet: evidence for a transition from oceanic to continental subduction. Journal of Petrology 44 (10), 1833–1865.

Dupont-Nivet, G., Krijgsman, W., Langereis, C.G., Abels, H.A., Dai, S., Fang, X.M., 2007. Tibetan plateau aridification linked to global cooling at the Eocene–Oligocene transition. Nature 445, 635–638.

Edmond, J.M., 1992. Himalayan tectonics, weathering processes, and the strontium isotope record in marine limestones. Science 258, 1594–1597.

England, P., Houseman, G., 1989. Extension during continental convergence, with application to the Tibetan Plateau. Journal of Geophysical Research 94, 17561–17579.

Gao, S., Rudnick, R.L., Yuan, H.L., Liu, X.M., Liu, Y.S., Xu, W.L., Ling, W.L., Ayers, J., Wang, X.C., Wang, Q.H., 2004. Recycling lower continental crust in the North China craton. Nature 432, 892–897.

Gao, Y.F., Hou, Z.Q., Kamber, B.S., Wei, R.H., Meng, X.J., Zhao, R.S., 2007. Adakite-like porphyries from the southern Tibetan continental collision zones: evidence for slab melt metasomatism. Contributions to Mineralogy and Petrology 153 (1), 105–120.

Gao, Y.F., Wei, R.H., Hou, Z.Q., Tian, S.H., Zhao, R.S., 2008. Eocene high-MgO volcanism in southern Tibet: new constraints for mantle source characteristics and deep processes. Lithos 105, 63–72.

Garzione, C.N., Dettman, D.L., Quade, J., DeCelles, P.G., Butler, R.F., 2000. High times on the Tibetan Plateau: paleoelevation of the Thakkhola graben, Nepal. Geology 28 (4), 339–342.

Geng, Q.R., Pan, G.T., Zheng, L.L., Chen, Z.L., Fisher, R.D., Sun, Z.M., Qu, C.S., Dong, H., Wang, X.W., Li, S., Lou, X.Y., Fu, H., 2006. The Eastern Himalayan syntaxis: major tectonic domains, ophiolitic melanges and geologic evolution. Journal of Asian Earth Sciences 27 (3), 265–285.

Griffin, W.L., Pearson, N.J., Belousova, E., Jackson, S.E., O'Reilly, S.Y., van Achterberg, E., Shee, S.R., 2000. The Hf-isotope composition of cratonic mantle: LAM-MC-ICPMS analysis of zircon megacrystas in kimberlites. Geochimica et Cosmochimica Acta 64, 133–147.

Griffin, W.L., Wang, X., Jackson, S.E., Pearson, N.J., O'Reilly, S.Y., Xu, X.S., Zhou, X.M., 2002. Zircon chemistry and magma mixing, SE China: in-situ analysis of Hf isotopes, Tonglu and Pingtan igneous complexes. Lithos 61, 237–269.

Guillot, S., Maheo, G., de Sigoyer, J., Hattori, K.H., Pecher, A., 2008. Tethyan and Indian subduction viewed from the Himalayan high- to ultrahigh-pressure metamorphic rocks. Tectonophysics 451, 225–241.

Guo, Z., Wilson, M., Liu, J., 2007. Post-collisional adakites in south Tibet: products of partial melting of subduction-modified lower crust. Lithos 96, 205–224.

Harris, N.B.W., Xu, R.H., Lewis, C.L., Hawkesworth, C.J., Zhang, Y.Q., 1988. Isotope geochemistry of the 1985 Tibet Geotraverse, Lhasa to Golmud. Philosophical Transactions of the Royal Society of London, Series A 327, 263–285.

Hou, Z.Q., Gao, Y.F., Qu, X.M., Rui, Z.Y., Mo, X.X., 2004. Origin of adakitic intrusives generated during mid-Miocene east–west extension in southern Tibet. Earth and Planetary Science Letters 220 (1–2), 139–155.

Jiang, W., Mo, X.X., Zhao, C.H., Guo, T.Y., Zhang, S.Q., 1999. Geochemistry of granitoid and its mafic microgranular enclave in Gangdise belt, Qinghai–Xizang Plateau. Acta Petrologica Sinica 15, 89–97 (in Chinese with English abstract).

Jiang, Y.H., Jiang, S.Y., Ling, H.F., Dai, B.Z., 2006. Low-degree melting of a metasomatized lithospheric mantle for the origin of Cenozoic Yulong monzogranite-porphyry, east Tibet: geochemical and Sr–Nd–Pb–Hf isotopic constraints. Earth and Planetary Science Letters 241 (3–4), 617–633.

Jin, Y., McNutt, M.K., Zhu, Y.S., 1996. Mapping the descent of Indian and Eurasian plates beneath the Tibetan Plateau from gravity anomalies. Journal of Geophysical Research-Solid Earth 101 (B5), 11275–11290.

Kapp, P., Murphy, M.A., Yin, A., Harrison, T.M., Ding, L., Guo, J.H., 2003. Mesozoic and Cenozoic tectonic evolution of the Shiquanhe area of western Tibet. Tectonics 22 (1029). doi:10.1029/2001TC001332.

Kapp, P., Yin, A., Harrison, T.M., Ding, L., 2005. Cretaceous–Tertiary shortening, basin development, and volcanism in central Tibet. Geological Society of America Bulletin 117 (7–8), 865–878.

Kay, R., 1978. Aleutian magnesian andesites: melts from subducted Pacific ocean crust. Journal of Volcanology and Geothermal Research 4 (1–2), 117–132.

Kay, S.M., Ramos, V.A., Marquez, M., 1993. Evidence in Cerro-Pampa volcanic-rocks for slab-melting prior to ridge–trench collision in southern South-America. Journal of Geology 101 (6), 703–714.

Klootwijk, C., Gee, J., Peirce, J., Smith, G., McFadden, P., 1992. An early India–Asia contact: paleomagnetic constraints from Ninetyeast Ridge, ODP Leg 121. Geology 20 (5), 395–398.

Kohn, M.J., Parkinson, C.D., 2002. Petrologic case for Eocene slab breakoff during the Indo-Asian collision. Geology 30 (7), 591–594.

Lee, H.Y., Chung, S.L., Wang, Y.B., Zhu, D.C., Yang, J.H., Song, B., Liu, D.Y., Wu, F.Y., 2007. Age, petrogenesis and geological significance of the Linzizong volcanic successions in the Linzhou basin, southern Tibet: evidence from zircon U–Pb dates and Hf isotopes. Acta Petrologica Sinica 23, 493–500 (in Chinese with English abstract).

Leech, M.L., Singh, S., Jain, A.K., Klemperer, S.L., Manickavasagam, R.M., 2005. The onset of India–Asia continental collision: early, steep subduction required by the timing of UHP metamorphism in the western Himalaya. Earth and Planetary Science Letters 234 (1–2), 83–97.

Li, S.G., 2004. Exhumation mechanism of the ultrahigh-pressure metamorphic rocks in the Dabie mountains and continental collision process between the North and South China blocks. Earth Science Frontiers 11, 63–70 (in Chinese with English abstract).

Liao, Z.L., Mo, X.X., Pan, G.T., Zhu, D.C., Wang, L.Q., Jiang, X.S., Zhao, Z.D., 2007. Spatial and temporal distribution of peraluminous granites in Tibet and their tectonic significance. Journal of Asian Earth Sciences 29 (2–3), 378–389.

Liu, Y., Zhong, D., 1997. Petrology of high-pressure granulites from the eastern Himalayan syntaxis. Journal of Metamorphic Geology 15 (4), 451–466.

Liu, Y., Siebel, W., Massonne, H.J., Xiao, X.C., 2007a. Geochronological and petrological constraints for tectonic evolution of the central Greater Himalayan Sequence in the Kharta area, southern Tibet. Journal of Geology 115 (2), 215–230.

Liu, Y., Yanc, Z.Q., Wang, M., 2007b. History of zircon growth in a high-pressure granulite within the eastern Himalayan syntaxis, and tectonic implications. International Geology Review 49 (9), 861–872.

Ludwig, K., 2003. User's manual for Isoplot 3.0: a geochronological toolkit for Microsoft Excel. Berkeley Geochronology Center Special publication 4, 1–77.

Maheo, G., Guillot, S., Blichert-Toft, J., Rolland, Y., Pecher, A., 2002. A slab breakoff model for the Neogene thermal evolution of South Karakorum and South Tibet. Earth and Planetary Science Letters 195 (1–2), 45–58.

Miller, C., Schuster, R., Klotzli, U., Frank, W., Purtscheller, F., 1999. Post-collisional potassic and ultrapotassic magmatism in SW Tibet: geochemical and Sr–Nd–Pb–O isotopic constraints for mantle source characteristics and petrogenesis. Journal of Petrology 40 (9), 1399–1424.

Mo, X.X., Zhao, Z.D., Deng, J.F., Dong, G.C., Zhou, S., Guo, T.Y., Zhang, S.Q., Wang, L.L., 2003. Response of volcanism to the India–Asia collision. Earth Science Frontiers 10, 135–148 (in Chinese with English abstract).

Mo, X.X., Hou, Z.Q., Niu, Y.L., Dong, G.C., Qu, X.M., Zhao, Z.D., Yang, Z.M., 2007. Mantle contributions to crustal thickening during continental collision: evidence from Cenozoic igneous rocks in southern Tibet. Lithos 96 (1–2), 225–242.

Mo, X.X., Niu, Y.L., Dong, G.C., Zhao, Z.D., Hou, Z.Q., Zhou, S., Ke, S., 2008. Contribution of syncollisional felsic magmatism to continental crust growth: a case study of the Paleogene Linzizong volcanic Succession in southern Tibet. Chemical Geology 250 (1–4), 49–67.

Molnar, P., England, P., Martinod, J., 1993. Mantle dynamics, uplift of the Tibetan plateau, and the Indian monsoon. Reviews of Geophysics 31 (4), 357–396.

Molnar, P., Houseman, G.A., Conrad, C.P., 1998. Rayleigh–Taylor instability and convective thinning of mechanically thickened lithosphere: effects of non-linear

viscosity decreasing exponentially with depth and of horizontal shortening of the layer. Geophysical Journal International 133 (3), 568–584.
Nomade, S., Renne, P.R., Mo, X., Zhao, Z., Zhou, S., 2004. Miocene volcanism in the Lhasa block, Tibet: spatial trends and geodynamic implications. Earth and Planetary Science Letters 221 (1–4), 227–243.
Owens, T.J., Zandt, G., 1997. Implications of crustal property variations for models of Tibetan plateau evolution. Nature 387, 37–43.
Pan, G.T., Mo, X.X., Hou, Z.Q., Zhu, D.C., Wang, L.Q., Li, G.M., Zhao, Z.D., Geng, Q.R., Liao, Z.L., 2006. Spatial–temporal framework of the Gangdese Orogenic Belt and its evolution. Acta Petrologica Sinica 22, 521–533 (in Chinese with English abstract).
Powell, C.M., 1986. Continental underplating model for the rise of the Tibetan Plateau. Earth and Planetary Science Letters 81 (1), 79–94.
Prell, W.L., Kutzbach, J.E., 1992. Sensitivity of the Indian monsoon to forcing parameters and implications for its evolution. Nature 360, 647–652.
Qu, X.M., Hou, Z.Q., Li, Y.G., 2004. Melt components derived from a subducted slab in late orogenic ore-bearing porphyries in the Gangdese copper belt, southern Tibetan plateau. Lithos 74, 131–148.
Rapp, R.P., Watson, E.B., 1995. Dehydration melting of metabasalt at 8–32 kbar: implications for continental growth and crust-mantle recycling. Journal of Petrology 36, 891–931.
Raymo, M.E., Ruddiman, W.F., 1992. Tectonic forcing of later Cenozoic climate. Nature 359, 117–122.
Rodgers, A.T.J., Schwartz, S.Y., 1997. Low crustal velocities and mantle lithospheric variations in southern Tibet from regional Pnl waveforms. Geophysical Research Letters 24, 9–12.
Scherer, E., Munker, C., Mezger, K., 2001. Calibration of the lutetium–hafnium clock. Science 293, 683–687.
Schulte-Pelkum, V., Monsalve, G., Sheehan, A., Pandey, M.R., Sapkota, S., Bilham, R., Wu, F., 2005. Imaging the Indian subcontinent beneath the Himalaya. Nature 435, 1222–1225.
Spicer, R.A., Harris, N.B.W., Widdowson, M., Herman, A.B., Guo, S.X., Valdes, P.J., Wolfe, J.A., Kelley, S.P., 2003. Constant elevation of southern Tibet over the past 15 million years. Nature 421, 622–624.
Stern, C.R., Kilian, R., 1996. Role of the subducted slab, mantle wedge and continental crust in the generation of adakites from the Andean Austral volcanic zone. Contributions to Mineralogy and Petrology 123 (3), 263–281.
Sun, S., McDonough, W., 1989. Chemical and isotopic systematics of oceanic basalts: implications for mantle composition and processes. Geological Society London Special Publications 42 (1), 313–345.
Tapponnier, P., Xu, Z.Q., Roger, F., Meyer, B., Arnaud, N., Wittlinger, G., Yang, J.S., 2001. Oblique stepwise rise and growth of the Tibet plateau. Science 294, 1671–1677.
Tatsumi, Y., 2006. High-Mg andesites in the setouchi volcanic belt, Southwestern Japan: analogy to Archean magmatism and continental crust formation? Annual Review of Earth and Planetary Sciences 34, 467–499.
Tilmann, F., Ni, J., Team, I.I.S., 2003. Seismic imaging of the downwelling Indian lithosphere beneath central Tibet. Science 300, 1424–1427.
Turner, S., Nrnaud, N., Liu, J., Rogers, N., Hawkesworth, C., Harris, N., Kelley, S., van Calsteren, P., Deng, W., 1996. Post-collision, shoshonitic volcanism on the Tibetan plateau: implications for convective thinning of the lithosphere and the source of ocean island basalts. Journal of Petrology 37, 45–71.
Vervoort, J.D., Blichert-Toft, J., 1999. Evolution of the depleted mantle: Hf isotope evidence from juvenile rocks through time. Geochimica et Cosmochimica Acta 63 (3–4), 533–556.
Wen, D.R., Liu, D.Y., Chung, S.L., Chu, M.F., Ji, J.Q., Zhang, Q., Song, B., Lee, T.Y., Yeh, M.W., Lo, C.H., 2008. Zircon SHRIMP U–Pb ages of the Gangdese Batholith and implications for Neotethyan subduction in southern Tibet. Chemical Geology 252, 191–201.
Williams, H., Turner, S., Kelley, S., Harris, N., 2001. Age and composition of dikes in Southern Tibet: new constraints on the timing of east–west extension and its relationship to postcollisional volcanism. Geology 29 (4), 339–342.
Williams, H.M., Turner, S.P., Pearce, J.A., Kelley, S.P., Harris, N.B.W., 2004. Nature of the source regions for post-collisional, potassic magmatism in Southern and Northern Tibet from geochemical variations and inverse trace element modelling. Journal of Petrology 45, 555–607.
Yin, A., 2006. Cenozoic tectonic evolution of the Himalayan orogen as constrained by along-strike variation of structural geometry, exhumation history, and foreland sedimentation. Earth Science Reviews 76, 1–131.
Yin, A., Harrison, T.M., 2000. Geologic evolution of the Himalayan–Tibetan orogen. Annual Review of Earth and Planetary Sciences 28, 211–280.
Yuan, H.L., Gao, S., Liu, X.M., Li, H.M., Gunther, D., Wu, F.Y., 2004. Accurate U–Pb age and trace element determinations of zircon by laser ablation-inductively coupled plasma-mass spectrometry. Geostandards and Geoanalytical Research 28, 353–370.
Yuan, H.L., Gao, S., Dai, M.L., Zong, C.L., Gunther, D., Fontaine, G.H., Liu, X.M., Diwu, C.R., 2008. Simultaneous determinations of U–Pb age, Hf isotopes and trace element compositions of zircon by excimer laser-ablation quadrupole and multiple-collector ICP-MS. Chemical Geology 247, 100–118.
Yue, Y.H., Ding, L., 2006. $^{40}Ar/^{39}Ar$ geochronology, geochemical characteristics and genesis of the Linzhou basic dikes, Tibet. Acta Petrologica Sinica 22, 855–866 (in Chinese with English abstract).
Zhang, H.F., Gao, S., Zhong, Z.Q., Zhang, B.R., Zhang, L., Hu, S.H., 2002. Geochemical and Sr–Nd–Pb isotopic compositions of Cretaceous granitoids: constraints on tectonic framework and crustal structure of the Dabieshan ultrahigh-pressure metamorphic belt, China. Chemical Geology 186, 281–299.
Zhang, H.F., Xu, W.C., Zhong, K.Q., Cai, H.M., Yuan, H.L., 2007a. Zircon U–Pb and Hf isotopic composition of deformed granite in the southern margin of the Gangdese belt, Tibet: evidence for early Jurassic subduction of Neo-Tethyan oceanic slab. Acta Petrologica Sinica 23, 1347–1353 (in Chinese with English abstract).
Zhang, H.F., Xu, W.C., Guo, J.Q., Zhong, K.Q., Cai, H.M., Yuan, H.L., 2007b. Indosinian orogenesis of the Gangdise Terrane: evidences from zircon U–Pb dating and petrogenesis of granitoids. Earth Science-Journal of China University of Geosciences 32, 155–166 (in Chinese with English abstract).
Zhang, Z.M., Zheng, L.L., Wang, J.L., Zhao, X.D., Shi, C., 2007c. Garnet pyroxenite in the Namjabarwa Group-complex in the eastern Himalayan tectonic syntaxis, Tibet, China: evidence for subduction of the Indian continent beneath the Eurasian plate at 80–100 km depth. Geological Bulletin of China 26, 1–12 (in Chinese with English abstract).
Zhao, W., Morgan, W., 1987. Injection of Indian crust into Tibetan lower crust: a two-dimensional finite element model study. Tectonics 6, 489–504.
Zhong, D.L., Ding, L., 1996. Discovery of high-pressure basic granulite in Namjagbarwa area, Tibet, China. Chinese Science Bulletin 41, 87–88.
Zhu, D.C., Pan, G.T., Mo, X.X., Wang, L.Q., Liao, Z.L., Zhao, Z.D., Dong, G.C., Zhou, C.Y., 2006. Late Jurassic–Early Cretaceous geodynamic setting in middle-northern Gangdese; new insights from volcanic rocks. Acta Petrologica Sinica 22, 534–546 (in Chinese with English abstract).
Zhu, D.C., Pan, G.T., Chung, S.L., Liao, Z.L., Wang, L.Q., Li, G.M., 2008. SHRIMP zircon age and geochemical constraints on the origin of lower Jurassic volcanic rocks from the Yeba formation, Southern Gangdese, south Tibet. International Geology Review 50 (5), 442–471.